Effect of bubble behaviour on the performance of a zero-gap chlor-alkali electrolyzer

Lentjes, Dion S.

Award date:
2022

Department of Chemical Engineering
Sustainable Process Engineering Research Group

Effect of bubble behaviour on the performance of a zero-gap chlor-alkali electrolyzer

Msc Thesis

Dion Lentjes

Date: 07-07-2022

Graduation supervisor: prof. dr. ir. J. van der Schaaf

External committee member: dr.ir K.A. Buist

Daily supervisor: PDEng. MSc R. Lira Garcia Barros, MSc N. Guruprasad and dr. C.F. Gomez

Committee member: dr.ir M.T. de Groot

Abstract

To further intensify chlor-alkali membrane electrolysis, a better understanding on the bubble behavior is required. In this work, video analysis of bubble behavior inside a zero-gap chlor-alkali cell is performed. The electrochemical performance is also evaluated in order to correlate the cell performance with bubble dynamics. By using a transparent Nafion 117, it is possible to observe the bubble behavior between the electrode and membrane in a zero-gap configuration, which is (currently) unseen in literature. Due to the high solubility of chlorine, which results in significantly less bubble formation, mostly the hydrogen bubble behavior was analyzed. This can also help with gaining a better understanding about the behavior of alkaline water electrolysis, because of the similarities for the cathodic side of the processes.

It was found that the bubble behavior inside a zero-gap configuration can significantly differ per position, which is most likely caused by the inconsistent distance between the electrode and membrane along the cell. The following phenomena were observed: bubble curtain, bubble froth, static bubbles between the electrode and the membrane as well as bubbles / gas films sliding to the rim of the openings in the cathode. Also larger bubbles with diameters over 3 mm are observed in the openings of the cathode which leave gas pocket behind upon detachment. The bubble effects appear to be more significant for hydrogen as compared to chlorine, which is in agreement with literature. This effect is most likely caused by the higher surface tension of the catholyte as compared to the anolyte. These effects might cause an increase in resistance, causing part of the current to flow via the backside of the electrodes, which leads to the reaction also taking place at the backside of the electrodes. However, this is not certain, since it might also be caused by the backside of the electrode taking longer to reach the desired supersaturation in order to initiate bubble growth at the backside of the electrode.

Since no properly calibrated high current potentiostat was available, the ohmic resistance of the electrolyzer could not be directly measured. Instead, the ohmic resistance was calculated by subtracting reversible cell potential and total activation overpotential (measured with potentiostat) from the cell potential (measured with power supply). Interestingly, even though bubbles are observed between the electrodes and the membrane, the ohmic resistance remains constant at high current density (up to 1 A/cm^2). This suggest that the bubble effects do not (significantly) affect the ohmic resistance of the electrolyzer. It was also found that the ohmic resistance of the cell was higher than the membrane resistance of a Nafion 117 at 54 and 69°C reported by Sijabat et al in a NaOH-NaOH system. The experimentally found membrane resistance at 28°C was lower than the membrane resistance reported by Sijabat et al. This discrepancy could be either be due to inaccuracies in Sijbat's experiments, or the fact that the resistance of the Nafion 117 membrane is affected by the NaCl concentration.

An important recommendation is to improve the accuracy of measuring the membrane resistance, preferably in a NaOH-NaCl system. This allows for a more fair comparison between the ohmic resistance of the electrolyzer and the resistance of the membrane. Another recommendation is employing a high current potentiostat in order to to directly measure the ohmic resistance, instead of calculating.

Table of Contents

1. Introduction

1.1 Chlor-Alkali process

Electrochemical processes enable the production relevant chemicals or storage of energy in the form of chemicals such as hydrogen by the use of renewable energy [1][2]. Consequently, electrochemistry has gained an increasing amount of attention since the end of the 20^{th} century, as indicated by the increasing number of publications per year on this topic [3]. One of the oldest electrochemical industries is the chlor-alkali process, with some of the plants being opened as early as the 1890's [4]. Besides the fact that the chlor-alkali is one of the oldest electrochemical industries, it is also one of the largest. The chlor-alkali industry consumed over 150 TWh of electricity annually for the past few years, which is just slightly below 1% of the global annual electricity consumption [5][6][7]. The main product of the chlor-alkali industry is chlorine, of which the global annual production was approximately 80 million tonnes in 2020 [8]. Besides chlorine, this process also produces sodium hydroxide (caustic soda) and hydrogen, which are all considered to be valuable products. Lithium and potassium hydroxide can also be produced as products, however sodium hydroxide is the most common of these three. These products are produced according to the following half-reactions:

$$2\,\mathrm{Cl^-} \longrightarrow \mathrm{Cl_2} + 2\,\mathrm{e^-} \quad (E^0_{298K} = 1.36\mathrm{V_{vs\ SHE}}) \tag{1.1}$$

$$2\,\mathrm{H_2O} + 2\,\mathrm{e^-} \longrightarrow \mathrm{H_2} + 2\,\mathrm{OH^-} \quad (E^0_{298K} = -0.83\mathrm{V_{vs\ SHE}}) \tag{1.2}$$

With the first half-reaction occurring at the anode and the latter one occurring at the cathode. Both chlorine and caustic soda are used in a variety of industries such as construction, energy, food, health and transportation [9]. Chlorine is used for the production of plastics (such as PVC and PUR), solvents, fire protection and medical products, while caustic soda is utilized for the production of soaps and detergents, aluminium and pulp [9][10]. The produced hydrogen generally has a high purity (>99.9%), which allows it being used in applications that require high purity hydrogen such as the electronics industry, fertilizer production or fuel cells [11][12]. Unfortunately, 10 to 15% of the produced hydrogen is not used and is just released into the atmosphere, however the percentage of unused hydrogen is likely to decrease due to the expected increase in demand for hydrogen [13].

Originally, mainly mercury and diaphragm type of cells were used for the chlor-alkali process [14]. However, due to health related risks; mercury pollution by the mercury cells and use of asbestos for diaphragm cells, alternatives were required. Currently, the main employed cell type is the membrane cell, accounting for over 80% of the global chlor-alkali capacity [6]. A schematic of a chlor-alkali membrane cell is shown in figure 1.1.

A variety of cathode materials can be used for the hydrogen evolution reaction (HER) in alkaline media. Platinum offers the best HER performance, however it comes with the drawback of higher costs [6]. A cheaper alternative is, for example, nickel [6]. Dimensionally Stable Anode (DSA) have the best performance regarding the chlorine evolution reaction (CER). DSA's are titanium electrodes coated with Ir/Ru/Ti mixed metal oxides (MMO) [16]. At the anode, the formation of oxygen occurs as a side reaction according to the following half-reaction [16].

$$2\,\mathrm{H_2O} \longrightarrow \mathrm{O_2} + 4\,\mathrm{H^+} + 4\,\mathrm{e^-} \quad (E^0_{298K} = 1.23\mathrm{V_{vs\ SHE}}) \tag{1.3}$$

This unwanted side reaction will reduce the efficiency of the process. This will also lead to more energy being required during separation in order to obtain the desired chlorine purity [16]. The selectivity towards chlorine can be improved by, for example, acidifying the anolyte [16]. The anolyte and catholyte compartments are separated by a cation-exchange membrane (CEM). This membrane should allow the transport of sodium ions and hinder the transport of hydroxide and chloride ions. However, in practice it is found that only the chloride transport is negligible, whereas the hydroxide transport is still significant [17]. Another advantage of the membrane cell is the power consumption compared to the other technologies: on average 3700 kWh, 2900 kWh and

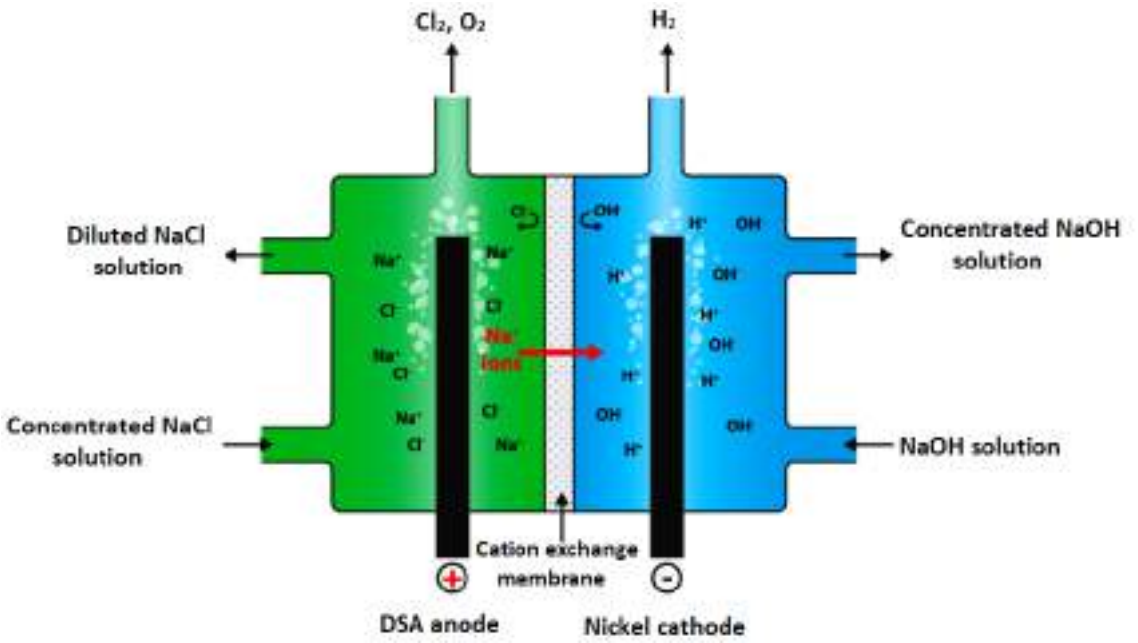

Figure 1.1: Schematic of chlor-alkali membrane cell. Concentrated NaCl is fed to anolyte compartment where chlorine and traces of oxygen are produced at the anode. The gaseous products and diluted NaCl exit the anolyte compartment. A NaOH solution is fed to the catholyte compartment where hydrogen is produced at the cathode. Hydrogen and concentrated NaOH exit the catholyte compartment. Sodium ions transport through the cation exchange membrane to complete the electrical circuit [15].

2500 kWh per metric ton chlorine for mercury, diaphragm and membrane cells respectively [18]. It should be noted however, that due to the fact that the power consumption depends on numerous of factors such as cell configuration, purity of raw materials, age of cell internals and the actual current density, the power consumption might deviate from values stated above [19]. The power consumption is determined by the current efficiency and the cell voltage. The cell voltage is the sum of the thermodynamic decomposition voltage, activation overpotentials and ohmic drops over the membrane, electrolytes and electrical circuit. In order to reduce the cell potential, the overpotentials and ohmic drops should be minimized.

1.2 Zero-gap cell configuration

One way to reduce the total ohmic drop is by employing a zero-gap configuration. This type of configuration was commercially utilized for the first time around the 1950's [20]. The difference between a finite or narrow gap and a zero-gap is the distance between the electrodes and the membrane. In a finite gap the electrodes are placed at a distance in the order of mm from the membrane. In a zero-gap, the membrane is sandwiched between two porous electrodes, reducing the distance between the electrodes to (practically) the thickness of the membrane, which is in the order of a few hundred microns [21][22]. This means that the ohmic drop over the electrolytes is nearly completely removed. Both configurations are depicted in Figure 1.2.

It should be mentioned that it is difficult to achieve a perfect zero-gap configuration [24]. Once a zero-gap configuration slightly deviates from the ideal configuration, it could result in a significant decrease in performance due to for example gas blanketing [24]. Using porous electrodes in zero-gap configuration allows bubbles to be transported from the side of the electrode facing the membrane towards the bulk of the electrolyte [23]. One important parameter to prevent bubbles getting trapped between the electrode and membrane is the hydrophilicity of the membrane. If the membrane has hydrophobic properties, a finite gap outperforms a zero-gap due to the fact that bubbles are more likely to get trapped between the electrode and membrane in a zero-gap configuration [25]. Therefore, membrane in zero-gap electrolyzers usually have hydrophilic coatings such as TiO_2 or ZrO_2 to counteract the bubble attachment [26]. Since the distance between

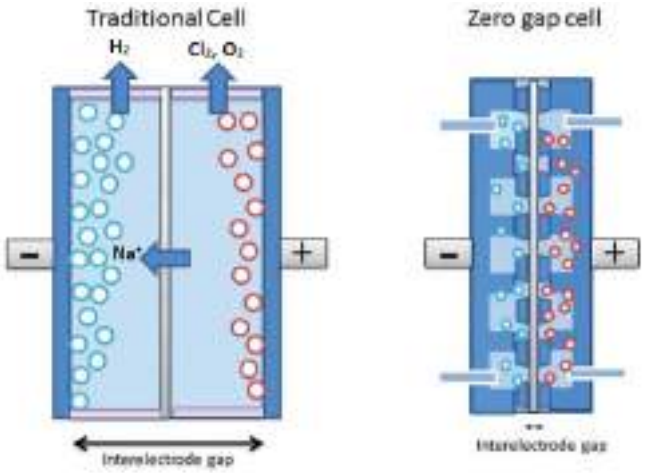

Figure 1.2: Finite gap configuration (left) and zero-gap configuration (right) [23].

the electrodes and the membrane is theoretically zero for a zero-gap, the total ohmic resistance should be equal to the ohmic resistance of the membrane. Additionally, since a low amount of gas should be present between the electrode and membrane, the ohmic resistance should not increase with current density. However, the ohmic resistance in zero-gap cells was consistently found to be significantly higher than the expected resistance [27].

1.3 Bubble effects

The fact that the ohmic resistance increases with current density, could indicate that bubble effects play a role [28]. Unfortunately, very little quantitative results on bubble effects in zero-gap systems are available in literature. Besides the fact that bubbles could play a role in increasing the ohmic resistance, there is another way bubbles could increase the cell potential. Bubbles attached to the electrode decrease the active electrode area, which consequently increases the activation overpotentials [29]. One can imagine that bubbles with small contact angles occupy a relatively small part of the electrode area and thus only a small fraction of the electrode area is unavailable for the reaction. Generally, it is accepted that the current density below adhering bubbles is quite small. This makes it valid to assume that the area shadowed by orthogonal projection of the contour of the attached bubbles is inactive [30]. However, Lake et al [31] contradicted this assumption by showing that the electrode area beneath attached bubbles is still (partly) active. Unfortunately, this effect is not quantified. At higher current densities, bubble effects are more pronounced and they become a limiting factor in the process [32]. To further intensify electrochemical processes, it is important to gain a better understanding in these bubble effects.

1.4 Scope and outline of the thesis

Since the literature on bubble effects in zero-gap electrolyzers is scarce, the goal of this thesis is to contribute to filling this knowledge gap. The objective is to gain better understanding in what type of bubble phenomena play a role and how they might affect cell performance, specifically for a zero-gap chlor-alkali cell. For this purpose, a transparent Nafion 117 membrane will be employed. This allows for visualization of the bubble behavior inside the gap, i.e. between the electrodes and the membrane. Besides the advantage of a transparent membrane, the chlor-alkali process has another inherent advantage regarding visual analysis over the alkaline water electrolysis process. At room temperature, the solubility of chlorine in brine is around $2.1 \cdot 10^{-2}$ mol/L at room temperature (see Appendix J.), whereas the solubility of oxygen in KOH (AWE uses a different anolyte) is around $1 \cdot 10^{-4}$ mol/L (see Appendix J.). This results in the fact that during startup of operation barely any gas is produced at the anode, especially when operating with a low current density and high flow rate. Consequently, when looking from the anodic side inside the gap, bubbles barely hinder the visibility. This means that the chlor-alkali system can also help answering questions for AWE systems, since the cathodic process has similarities for both processes. However, this also comes with a drawback, since a relatively small amount of chlorine is produced in the form of bubbles, the

bubble behavior of chlorine can be less extensively studied. The videos will then be compared with the electrochemical performance of the cell in order to determine whether the visual observations can explain the performance of the cell. Two measuring techniques will be used; polarization curve analysis as well as Electrochemical Impedance Spectroscopy (EIS).

2. Theory

2.1 Cell potential

The cell performance is often presented in the form of polarization (IV) curves. Generally, a typical trend for the cell potential is observed in this type of curves; the cell potential sharply increases at low current densities after which it reaches a linear regime for higher current densities. A typical polarization curve for a zero-gap chlor-alkali electrolyzer, including the different contributions, is depicted in the figure below.

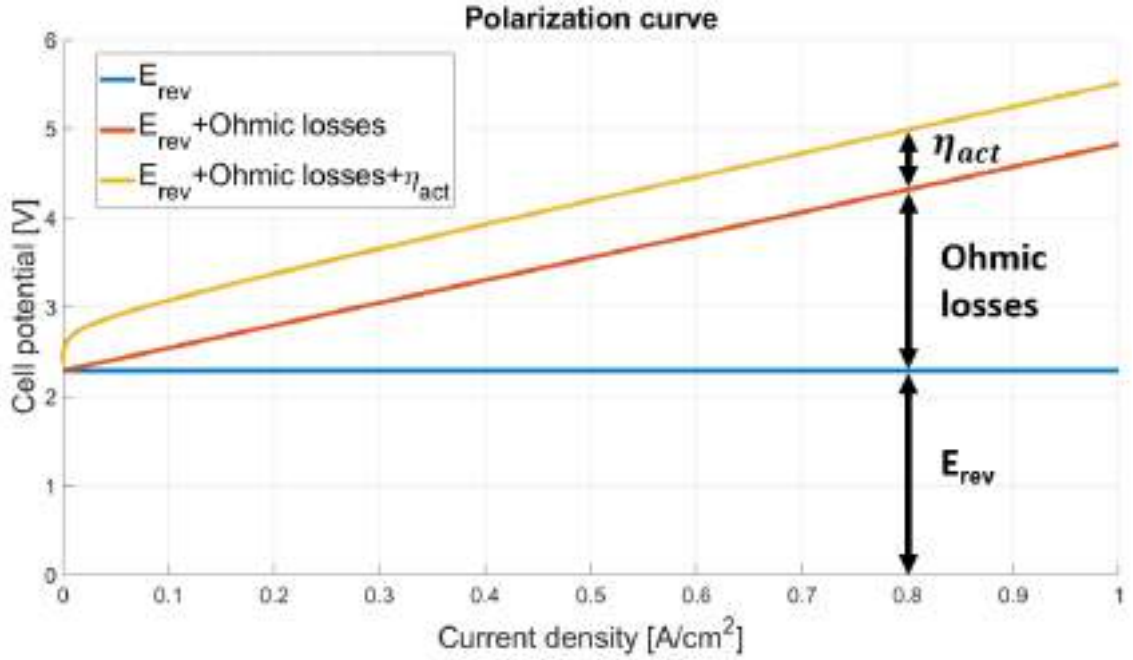

Figure 2.1: Typical polarization curve of a zero-gap chlor-alkali electrolyzer at 30°C, 25 wt% NaCl and 33 wt% NaOH. E_{rev} = 2.28, AR = 2.54 Ωcm^2, b_{tot} = 150 mV/dec and $I_0 = 10^{-5}$ A/cm^2.

This behavior can be explained by looking at the different contributions of the cell potential.

$$E_{cell} = E_{rev} + |\eta_C| + |\eta_A| + IAR_{an} + IAR_{cath} + IAR_{mem} \tag{2.1}$$

The steep slope at low current density originates from the logarithmic activation overpotential terms (see section 2.1.2) and the linear regime at higher current density originates from the ohmic contributions of the electrolytes and membrane (see sections 2.1.3 and 2.1.4). It is assumed that cable and contact resistances have an insignificant effect on the total cell pottential. To obtain the best cell performance, one should aim to minimize the cell potential. Since bubbles can affect the cell potential, it is important to get a better understanding of their effects. In the following sections the different contributions to the cell potential and the effects of bubbles on them will be discussed.

2.1.1 Reversible cell potential

The reversible cell potential is the minimum required voltage to induce the electrochemical reactions and can be expressed by the difference between the thermodynamic potential of the anode and cathode [33]. Since the reversible cell potential is an important parameter for polarization curve

fitting, it is essential to accurately describe this value.

$$E_{rev} = E_{0,A} - E_{0,C} \tag{2.2}$$

Where the thermodynamic potentials can be described with the Nernst equation.

$$E_{0,A} = E_A^0 + \frac{RT}{2F} ln\left(\frac{a_{Cl_2}}{(a_{Cl^-})^2}\right) \tag{2.3}$$

$$E_{0,C} = E_C^0 + \frac{RT}{2F} ln\left(\frac{a_{H_2O}}{a_{H_2}(a_{OH^-})^2}\right) \tag{2.4}$$

$E_C{}^0$ and $E_A{}^0$ are the standard electrode potentials of the cathodic and anodic reaction, respectively. Their temperature dependency was obtained from literature and can be found in Appendix A. [34]. These temperature dependent standard electrode potentials are compared with literature in order to ensure their validity [35][36][37]. The activity will be modelled differently, depending on the nature of the species, i.e. ion, solvent or gas. The activity of ionic species is described by the molality (m_i) and the activity coefficient on molality basis ($\gamma_{m,i}$).

$$a_i = \gamma_{m,i} m_i \tag{2.5}$$

For simple calculations, the activity coefficient is usually assumed to be equal to unity, however this only holds for ideal solutions. This assumption is acceptable for dilute solutions, but significantly deviates from reality for concentrated solutions [38][39]. Since the chlor-alkali process operates with concentrated electrolytes, it is important to implement an activity model that is able to describe the activity at these concentrations. Since it is difficult to measure and describe single-ion activities [40], the mean ionic activity coefficient will be used for the salts. This means that the mean ionic activity coefficient of NaCl will be used for the activity coefficient of Cl- and the mean ionic activity coefficient of NaOH will be used for the activity coefficient of OH-. For the the activity coefficient of Cl-, a modified Pitzer model is applied [41]. This model is able to describe the activity coefficient of NaCl up to a temperature of 100°C and a concentration of 6 molal [42][43].

$$ln(\gamma_{MX}^{\pm}) = |z_M z_X| f^{\gamma} + \left(\frac{2\nu_M \nu_X}{\nu_{MX}}\right) m B_{MX}^{\gamma} + \left(\frac{2(\nu_M \nu_X)^{3/2}}{\nu_{MX}}\right) m^2 C_{MX}^{\gamma} \tag{2.6}$$

$$f^{\gamma} = -A_{\phi}\left(\frac{I^{1/2}}{1 + b_{MX} I^{1/2}} + \frac{2}{b_{MX} ln(1 + b_{MX} I^{1/2})}\right) \tag{2.7}$$

$$B_{MX}^{\gamma} = 2B_{MX} \tag{2.8}$$

$$C_{MX}^{\gamma} = 3|z_M z_X|^{1/2} C_{MX} \tag{2.9}$$

$$B_{MX} = q_1 + q_2(T - T_r) + q_3(T^2 - T_r^2) + q_4(T^3 - T_r^3) + q_5(T^4 - T_r^4) \tag{2.10}$$

$$C_{MX} = q_6 + q_7(T - T_r) + q_8(T^2 - T_r^2) + q_9(T^3 - T_r^3) + q_{10}(T^4 - T_r^4) \tag{2.11}$$

In the equations above, T is the temperature in K and T_r is 298.15K. The required parameters b_{MX} and $q_{1\text{-}10}$ are given in Appendix C.

$$A_{\phi} = \frac{1}{3}\left(\frac{2\pi N_0 \rho_w}{1000}\right)^{1/2}\left(\frac{e^2}{\epsilon_w k_B T}\right)^{3/2} \tag{2.12}$$

According to Chen et al [44] the Debye-Hückel parameter, A_ϕ, for aqueous electrolyte systems can be described by the following equation.

$$\begin{aligned} A_{\phi} = {} & -61.44534 \exp\left(\frac{T - T_{ref}}{T_{ref}}\right) + 2.864468 \exp\left(\frac{T - T_{ref}}{T_{ref}}\right)^2 + 183.5379 \ln\left(\frac{T}{T_{ref}}\right) \\ & - 0.6820223(T - T_{ref}) + 7.875695 \cdot 10^{-4}(T^2 - T_{ref}^2) + 58.95788\left(\frac{T_{ref}}{T}\right) \end{aligned} \tag{2.13}$$

T is the temperature in K and T_{ref} is 273.15K.

For the mean activity coefficient of NaOH, an alternative model was employed [45], since the modified Pitzer model above fails to accurately describe the mean activity coefficient of NaOH.

Even though the model is based on data up to only 70C and 12.2 molal, it able to predict the activity coefficient of NaOH up to 100C and 14 molal when comparing it with other literature [46][42].

$$log(\gamma^{\pm}_{MX}) = -\frac{u\sqrt{m}}{1+\sqrt{2m}} + Bm + Cm^2 + Dm^3 + Em^4 \tag{2.14}$$

$$B = 6.519 \cdot 10^{-3} + 1.5995 \cdot 10^{-3} T_c - 1.8327 \cdot 10^{-5} T_c^2 \tag{2.15}$$

$$C = 1.3713 \cdot 10^{-} - 5.0071 \cdot 10^{-4} T_c + 5.6385 \cdot 10^{-6} T_c^2 \tag{2.16}$$

$$D = 5.994 \cdot 10^{-4} + 5.0215 \cdot 10^{-5} T_c - 6.4754 \cdot 10^{-7} T_c^2 \tag{2.17}$$

$$E = 5.96 \cdot 10^{-6} - 1.8056 \cdot 10^{-6} T_c + 2.4073 \cdot 10^{-8} T_c^2 \tag{2.18}$$

u is the universal constant of the Debye-Hückel limiting law, which is given by [47]:

$$u = 1.8143 \cdot 10^{6} (\epsilon_w T)^{-3/2} \tag{2.19}$$

With ϵ_w being the dielectric constant of the solvent, which is water is this case. This parameter is temperature dependent and can be described with the following empirical correlation [48].

$$\epsilon_w = 87.740 - 0.40008 T_c + 9.398 \cdot 10^{-4} T_c^2 - 1.410 \cdot 10^{-6} T_c^3 \tag{2.20}$$

For simple calculations, the activity of water is assumed to be unity, however this is inaccurate for concentrated electrolytes. Therefore the activity of water should be calculated accordingly. Using the same values for B, C, D, E and u the activity for water in NaOH can be described by the following equation for concentrations up to 12 molal NaOH and temperatures up to 100°C.

$$\begin{aligned} log(a_{H_2O}) = &-\frac{2m_{NaOH}}{log(10) \cdot 55.51} + \frac{u}{55.51\sqrt{2}} \\ &\left((1 + \sqrt{2m_{NaOH}} - 2ln(1 + \sqrt{2m_{NaOH}} - \frac{1}{1+\sqrt{2m_{NaOH}}} \right) \\ &- \frac{2}{55.51} \left(\frac{B m_{NaOH}^2}{2} + \frac{2C m_{NaOH}^3}{3} + \frac{3D m_{NaOH}^4}{4} + \frac{4E m_{NaOH}^5}{5} \right) \end{aligned} \tag{2.21}$$

For the activity of gaseous species, the gasses are assumed to behave ideally. This allows for the activity to be set equal to their partial pressure [49].

$$a_i = P_i \tag{2.22}$$

It is also assumed that the vapor phase is saturated with water. Correction factors proposed in literature to compensate for the vapor pressure lowering effect due to the presence of solutes, are also implemented [50].

$$P_{Cl_2} = P^A_{total} - \frac{1}{750} P^{sat}_{H_2O} (1 - R_{NaCl} m) \tag{2.23}$$

$$R_{NaCl} = (m-3) \cdot (1.9772 \cdot 10^{-3} - 1.193 \cdot 10^{-5} T_c) + 0.035 \tag{2.24}$$

$$P_{H_2} = P^C_{total} - \frac{1}{750} P^{sat}_{H_2O} (1 - R_{NaOH} m) \tag{2.25}$$

$$\begin{aligned} R_{NaOH} = &\, 3.170 \cdot 10^{-2} + (174 - T_c) \\ &\cdot (-8.6715 \cdot 10^{-5} + 3.368 \cdot 10^{-5} m - 1.354 \cdot 10^{-6} m^2 + \frac{7.88 \cdot 10^{-5}}{m}) \end{aligned} \tag{2.26}$$

The 1/750 factor in the second terms originates from the conversion of the saturation pressure of pure water as given by Antoine's equation from mmHg to bar [51].

$$P^{sat}_{H_2O} = 10^{A - B/(T_c + C)} \tag{2.27}$$

The activity corrected thermodynamic potentials can be compared with the ideal case, i.e. the case in which the activity of water is unity and the activity of ions is equal to their molality.

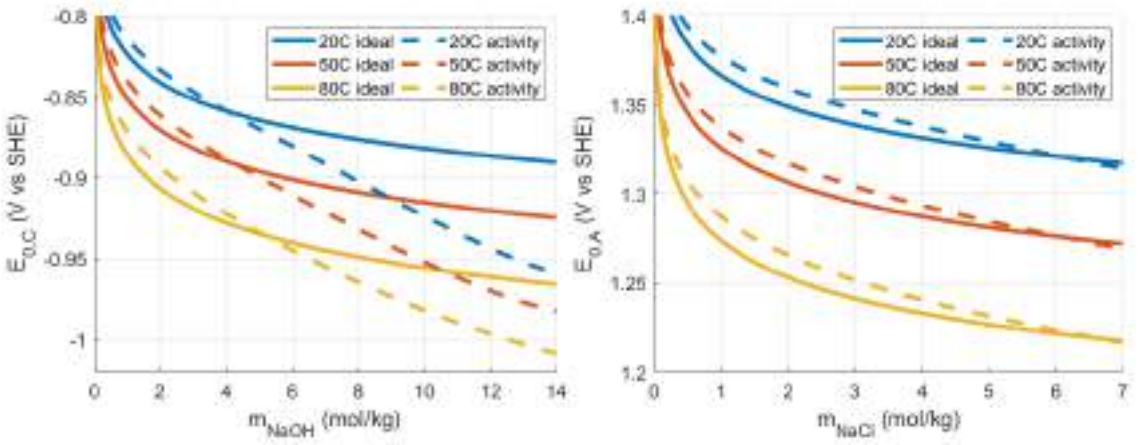

Figure 2.2: Comparison between thermodynamic potential according to the activity model and assuming ideality for hydrogen evolution (left) and chlorine evolution (right) versus molality.

It can be seen that the thermodynamic potential for chlorine evolution in the activity model case does not deviate from the ideal case significantly in the given concentration range. Especially for the industrially relevant NaCl concentration, the values are very similar. This can be explained by the fact that the activity coefficient of Cl- is relatively close to unity. The activity coefficient for NaOH on the other hand deviates significantly from unity, which causes the thermodynamic potential for hydrogen evolution to differ significantly between the two cases. This effect is mostly pronounced at higher concentrations. Differences up to 7.7% (69 mV) were found at the highest concentration. A similar comparison can be made with respect to temperature. This comparison will be made at the desired operation concentrations; 12 molal (32.4wt%) and 5.5 molal (24.3wt%) for NaOH and NaCl, respectively.

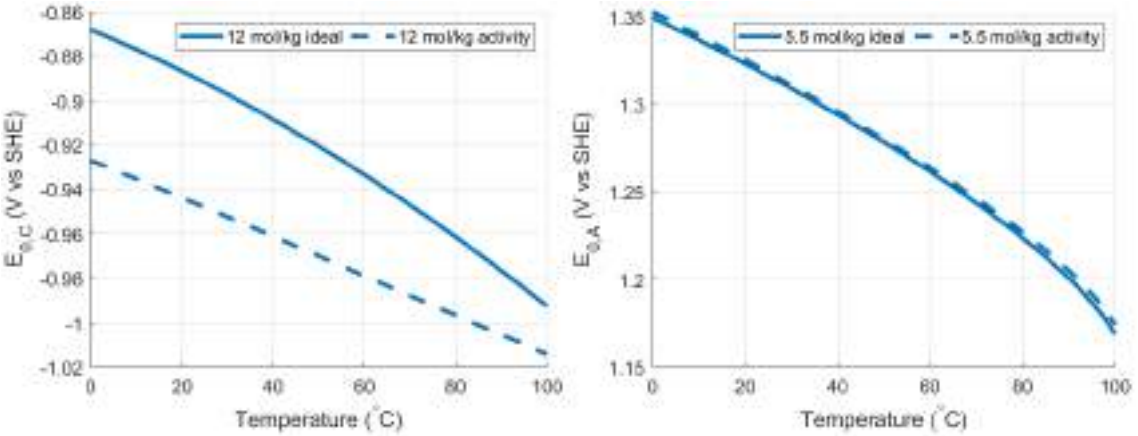

Figure 2.3: Comparison between thermodynamic potential according to the activity model and assuming ideality for hydrogen evolution (left) and chlorine evolution (right) versus temperature at industrially relevant concentration.

When comparing the thermodynamic potentials of both half reactions with values found in the Handbook of chlor-alkali technology, similar values are obtained [38]. It can be seen that there is practically no difference between the activity model and the ideal case for the chlorine evolution reaction. This can be explained by the fact that the activity coefficient of Cl- is relatively similar to unity at 5.5 molal over the entire temperature range. For NaOH significant differences are observed. At low temperature the difference is 6.8% (59mV), however at 80C this difference is reduced to 3.7% (35mV).
Bubbles can have an effect on the reversible cell potential. From equations 2.3 and 2.4 can be seen that the activities, and thus the concentrations play a role in the reversible cell potential. The

growth and detachment of bubbles induce convection and turbulence, which promotes mixing. This way the reactants near the surface of the electrode are replenished and products are transported to the bulk. Additionally, the bubbles act as a sink for the products, which lowers the concentration of the product at the electrode surface. All these phenomena have a lowering effect on the reversible potential. However, since it is assumed that the concentration of the reactants in the vicinity of the electrode is equal to the bulk concentration, the effect of bubbles on the reversible cell potential will be considered negligible.

2.1.2 Activation overpotentials

The activation overpotential is the required potential above the equilibrium potential to produce a certain current that depends on the activation energy of the electrochemical reaction [52]. Typically, the Butler-Volmer equation can be applied to correlate the current density to the activation overpotential [53]. This equation describes the net current density of an electrode by combining the current density of the oxidation reaction and the reduction reaction as indicated by the two exponential terms in the equation below [54]. This equation is valid under the assumption that the concentration of the reactant near the surface of the electrode is similar to the concentration in the bulk.

$$I = I_0 \left(\exp\left(\frac{\alpha_a n F \eta}{RT} \right) - \exp\left(\frac{-\alpha_c n F \eta}{RT} \right) \right) \tag{2.28}$$

Once the the overpotential is sufficiently high, $\eta >> \frac{RT}{nF}$ for the anode and $\eta << -\frac{RT}{nF}$ for the cathode, the forward reaction becomes dominant and the reverse reaction is assumed to be negligible. Then one of the exponents can be considered negligible as well and the equation can be simplified to the Tafel equation [28].

$$|\eta| = b \; log\left(\frac{I}{I_0} \right) \tag{2.29}$$

Where b is the Tafel slope, which depends on the reaction mechanism. The electron transfer coefficient α and exchange current density I_0 are functions of multiple parameters such as electrolyte concentration, pH, temperature and electrode material [55][54]. Values for these parameters and their corresponding experimental conditions (if provided) are tabulated below.

Catalyst	b (mV/dec)	I_0 (A/cm^2)	η^a (mV)	T (K)	c (mol/L)	pH (-)	I (A/cm^2)
TiO_2+RuO_2 [56]	28	$1.2 \cdot 10^{-3}$	53.7	368	5	3.5	10^{-3} - 10^{-1}
TiO_2+RuO_2+TiO_2[57]	43.1	-	-	333	5	2	10^{-3} - 10^{-1}
TiO_2+RuO_2+TiO_2 [57]	40.8	-	-	353	5	2	10^{-3} - 10^{-1}
TiO_2+RuO_2 [58]	40	$1.3 \cdot 10^{-7}$	235	343	5.13	-	10^{-4} - 10^{-2}
TiO_2+RuO_2[59]	45	-	-	343	5.13	-	10^{-4} - 10^{-2}
$Ru_{0.3}Pt_{0.7}O_2$ [60]	31	-	-	298	5	2	10^{-4} - 10^{-2}
RuO_2[61]	32.7	$5.1 \cdot 10^{-3}$	42.1	360	5.13	2	10^{-3} - 10^{-1}
IrO_2 [38]	40	$1.2 \cdot 10^{-3}$	76.7	298	5	2	10^{-4} - 10^{-2}

Table 2.1: Tafel slope and exchange current density for chlorine evolution reaction under different experimental conditions. All catalysts are deposited on titanium electrodes.
[a]The overpotential is tabulated at a current density of 0.1 A/cm^2

Electrode	b (mV)	I_0(A/cm^2)	η^a (mV)	T (K)	c (mol/L)	pH	I (A/cm^2)
Ni [62]	-116	$7.6 \cdot 10^{-7}$	593	293	1 (NaOH)	14.17	10^{-3} - 10^{-1}
Ni [63]	-144	$8.2 \cdot 10^{-6}$	588	323	1 (NaOH)	13.26	10^{-3} - 10^{-1}
Ni [64]	-121	$7.4 \cdot 10^{-5}$	378	298	1	13.89	10^{-2} - 10^{-1}
Ni [65]	-140	$1.1 \cdot 10^{-4}$	414	353	13	-	10^{-3} - 10^{-1}
Ni [66]	-90	$1 \cdot 10^{-5}$	360	-	4	-	10^{-5} - 10^{-2}
Pt [67]	-112	2.0	78	293	0.5	13	$10^{-0.3}$ - $10^{0.5}$
Pt [68]	-113	$6.3 \cdot 10^{-4}$	249	293	0.1	-	10^{-6} - 10^{-3}

Table 2.2: Tafel slope and exchange current density hydrogen evolution reaction under different experimental conditions. Concentrations are for KOH solutions, unless stated otherwise.
[a]The overpotential is tabulated at a current density of 0.1 A/cm^2

It is assumed that the Tafel slope and exchange current density are similar for NaOH and KOH. Since these quantities are system specific, they will be experimentally determined instead of taken from literature. This way a more meaningful insight in the bubble effects on the activation overpotentials can be obtained.
Once bubbles are being generated, they will block the active electrode area. The area that is in contact with gas is not available for reaction, therefore reducing the active electrode area. Consequently, this will increase the current density, since the current will be distributed over a smaller area. From equation 2.29 can be seen that this will result in an increase of the overpotential. The bubble coverage can be correlated to the activation overpotential by introducing the correction factor $(1 - \sigma)$ to take the reduction in active area into account.

$$|\eta| = b\ log\left(\frac{I_{actual}}{I_0}\right) = b\ log\left(\frac{I_{set}}{(1-\sigma)I_0}\right) \tag{2.30}$$

A lot research has been done on the bubble coverage [69][70][71]. It has been found that a wide variety of parameters can affect the bubble coverage, such as composition and flow of electrolyte, temperature, pressure, wettability of the electrodes and current density [72]. The proposed correlations between the bubble coverage and these parameters are empirical and often system specific, which makes it difficult to generalize them. Bubbles attached to the electrodes generally have small contact angles, meaning that only a small fraction of the gas is actually in contact with the electrode [73]. Typically, these bubble coverages are visually assessed with the aid of a (high speed) camera. The drawback of this technique is the fact that you have to assume that the area in the 'shadow' of the adhering bubbles is completely inactive, which is still debated. Models of current distributions under and in the vicinity of bubbles showed that this assumption is not valid and that the current density in the shadow of the bubble is still significant [74][75]. Recently, experiments agreeing with these models were carried out. The experiments indicated that the electrode area might be (partly) active [31]. According to these findings, figure 2.4 is the most representative way to illustrate the partial deactivation of the electrode area due to attached bubbles. This behavior adds even more to the complexity of quantifying the effects of bubbles on the activation overpotentials. Unfortunately, the author did not elaborate on this and the deactivating effect of the electrode area by the bubbles remains unquantified.

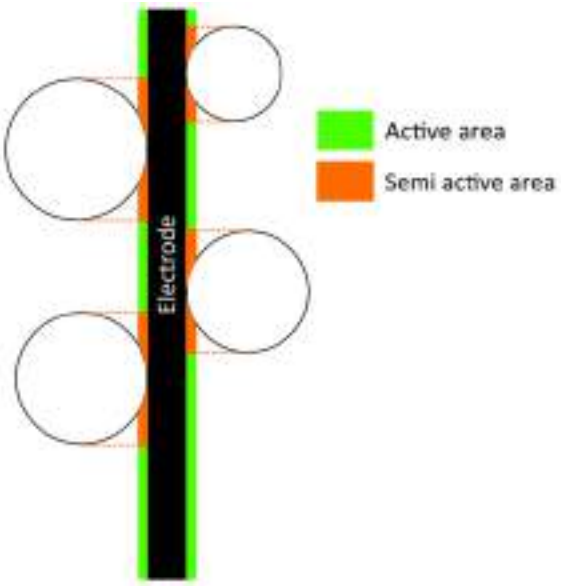

Figure 2.4: Electrode area in the shadow of the bubble is partly inactive due to bubble being attached.

2.1.3 Membrane resistance

Theoretically, the membrane resistance should be the only contributor to the ohmic resistance in a zero-gap configuration. In practice, however, the measured ohmic resistance is significantly higher [27]. The membrane resistance is dependent on its conductivity as well as its thickness.

$$R_{mem} = \frac{\delta_{mem}}{\kappa \cdot A} \tag{2.31}$$

Unfortunately, it is difficult to accurately determine the conductivity or resistance of the membrane, since both are a function of electrolyte concentration as well as temperature [76][77]. Literature on the conductivity or resistance of the used membrane (Nafion 117) is scarce, especially for binary systems such as the chlor-alkali process, which makes it even more difficult to accurately quantify them. According to experimental data from Chandran et al, the conductivity of a Nafion CEM is barely affected by the NaCl concentration and is basically controlled by the NaOH concentration [78]. Therefore, it is decided to use the experimental results from Sijabat et al for a Nafion-117 in a NaOH-NaOH (32 wt%) system [17] as reference values for the membrane resistance. Since Sijabat experimentally measured the resistance of the same membrane that is applied in this work with the same NaOH concentration, it is decided that Sijabat's experimental values are the most representative for this work. However, it should be noted that relatively high ohmic resistances are reported by Sijabat et al ($> 3\Omega cm^2$) at temperatures below 35°C. Additionally, a comparison will be made with alternative CEM resistances found in literature.

Membrane	T (K)	c_{an} (mol/L)	c_{cath} (wt%)	AR (Ω cm^2)
Nafion 901 [25]	358	2.9	23	1.2
Nafion 901 [79]	353	30wt% (NaOH)	30	3.0
CEM [33]	353	indep	indep	1.21
Nafion 117 [17]	353	32wt% (NaOH)	32	1.0
Aciplex F6801 [80]	363	3.3	32	0.85
Nafion 1200 EW [38]	298	30wt% (NaOH)	30	3.17[a]

Table 2.3: Chlor-alkali CEM area resistances.
[a] Assuming a membrane thickness of 0.019 cm.

Generally, the effect of bubbles on the membrane resistance is not mentioned in literature. This is most likely due to hydrophilic properties of the employed membranes and the consequent small

contact angles of the bubbles. Only when films of gas are formed between the electrode and the membrane, the membrane resistance might be affected by bubbles. Even though this effect might be unlikely to occur, it is important to consider it nonetheless. When bubbles are stuck between the membrane and the electrode, they increase the membrane resistance by blocking the pores and thus reducing the effective area for transport of ions. The hydrophobicity of the membrane is an important property with respect to this effect, since hydrophobic membranes could promote bubble attachment[25]. During this research only Nafion 117 membranes will be used, therefore the effect of different type of membranes on the bubble behavior will be deemed outside the scope. Since only the temperature dependency of membrane resistance is measured by Sijabat et al at two different NaOH concentrations (15 and 32 wt%), it is convenient to keep the catholyte concentration close to either of these values. Since industry operates generally at a NaOH concentration of around 30 wt%, it is decided to maintain the NaOH concentration around 32 wt%. Generally, an increase in ohmic resistance is found at higher current density, which might be caused by more bubbles being attached to the membrane due to the higher production rate [28].

2.1.4 Electrolyte resistances

The electrolyte resistances are the increases in cell potential induced by the electrolytes between the membrane and the electrode, since the gap in a zero-gap configuration is never zero in reality. The electrolyte resistance can be calculated with an equation that is equivalent to the one for the membrane resistance.

$$R_{electrolyte} = \frac{s}{\kappa \cdot A} \tag{2.32}$$

For a finite gap it makes sense to have an increase in ohmic resistance with increasing current density. Since bubbles are being released at the side of the electrode facing the membrane, the effective conductivity of the electrolyte is reduced according to, for example, the Bruggeman equation.

$$\frac{\kappa}{\kappa_0} = (1 - \epsilon_G)^{1.5} \tag{2.33}$$

An increasing trend in ohmic resistance with increasing current density is also observed for zero-gap cell configurations, albeit to a lesser extent [28]. To gain insight in the increasing ohmic resistance due to bubble effects, it is important to accurately calculate the conductivity of both electrolytes. The conductivity of NaCl is given by [81]:

$$\kappa_{NaCl} = (1.1 - 0.33\sqrt{m}) \cdot (\lambda \cdot m) \tag{2.34}$$

$$\lambda = 5.67 + 0.299T_c \tag{2.35}$$

And the conductivity of NaOH is given by:

$$\kappa_{NaOH} = A \cdot m + B \cdot m^2 + C \cdot m \cdot T + D \cdot \left(\frac{m}{T}\right) + E \cdot m^3 + F \cdot m^2 \cdot T^2 \tag{2.36}$$

The origin of this equation and the values of the coefficients are discussed in Appendix D. According to literature, the structure of the electrodes can also affect the ohmic resistance, probably due to difference in likelihood of bubble entrapment [28]. However, due to the compatibility with video analysis and time constraints, only expanded mesh electrodes will be used and the effect of different electrode morphologies will be deemed outside the scope of this research.

2.2 Force balance analysis

By performing a force balance analysis, the theoretical detachment radius of a freely growing bubble can be calculated. For this analysis, all forces acting on a bubble attached to a vertical plate electrode, as shown in Figure 2.5, are considered.

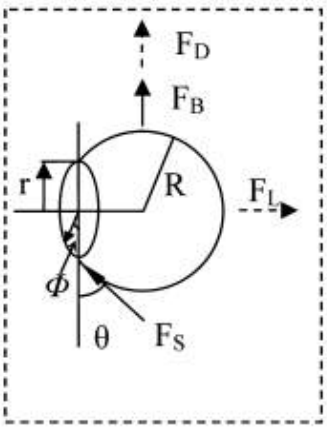

Figure 2.5: All forces acting on a bubble attached to a vertical surface [82].

It is assumed that bubbles detach due to the sum of the forces in the x-direction (direction parallel to the electrode) being non-zero rather than the sum of the forces in the y-direction (direction perpendicular to the electrode) being non-zero. The validity of this assumption was confirmed by Vervaecke [83]. A similar force balance analysis as proposed by Hoedemakers will be applied [84]. Hoedemakers considers the gravitational force, buoyancy force, tension force and drag force, all of which are relevant for this research.

The gravitational force is the force that pulls the bubble downwards and depends on the mass of the bubble. The mass of the bubble depends on the density of the gas and the volume of the bubble, for which a truncated spherical geometry is assumed. Since at room temperature less than 5% of the bubbles is water (see correlations in Section 2.1.1), the density of the bubbles are assumed to be equal to the the density of pure hydrogen and chlorine. The gasses are assumed to behave ideally.

$$F_g = -m_b g = -\frac{4}{3}\pi R^3 \frac{(1+cos\theta)^2(2-cos\theta)}{4}\rho_G g \tag{2.37}$$

The buoyancy force acts in an upwards direction and depends on the mass of the liquid that is displaced by the bubble. The density of both electrolytes can be found in Appendix H.

$$F_b = m_L g = \frac{4}{3}\pi R^3 \frac{(1+cos\theta)^2(2-cos\theta)}{4}\rho_L g \tag{2.38}$$

Due to the buoyancy force being larger than the gravitational force, the bubble will start to tilt. This tilting causes an advancing and receding angle, as shown in Figure 2.6. These angles are deviations ($\Delta\theta$) from the original contact angle.

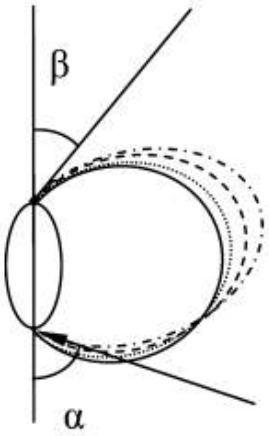

Figure 2.6: Advancing (α) and receding (β) angles of gas bubble attached to a vertical surface [82].

$$\alpha = \theta + \Delta\theta \tag{2.39}$$

$$\beta = \theta - \Delta\theta \tag{2.40}$$

The interfacial tension force is dependent on the surface tension, the contact area between the attached bubble and the electrode as well as the advancing and receding angle.

$$F_{s,x} = -2r\sigma \frac{\pi(\alpha - \beta)}{\pi^2 - (\alpha - \beta)^2}(sin\alpha + sin\beta) \tag{2.41}$$

$$r = Rsin\theta \tag{2.42}$$

When electrolyte flow is present in the system, a drag force in upward direction is exerted. This force depends the cross sectional area of the bubble that experiences the electrolyte flow, the velocity and density of the electrolyte as well as the drag coefficient.

$$F_d = \frac{1}{2}\pi R^2(1 - \frac{\theta - cos\alpha sin\theta)}{\pi}\rho_L v_L^2 C_D \tag{2.43}$$

The drag coefficient depends on the Reynolds number.

$$C_D = \frac{24}{Re} \quad \text{for} \quad Re < 0.1 \tag{2.44}$$

$$C_D = (\sqrt{\frac{24}{Re}} + 0.5407)^2 \quad \text{for} \quad 1 < Re < 500 \tag{2.45}$$

$$C_D = 0.44 \quad \text{for} \quad 500 \leq Re \leq 10^5 \tag{2.46}$$

Where the Reynolds number is defined as follows. The viscosity of both electrolytes can be found in Appendix I. The hydraulic diameter of the system is $6.47 \cdot 10^{-2}$ m.

$$Re = \frac{\rho_L v_L D_H}{\mu_L} \tag{2.47}$$

By setting the sum of all forces equal to 0, the theoretical detachment radius can be found.

$$0 = F_g + F_b + F_s + F_d \tag{2.48}$$

$$R = \frac{-b + \sqrt{b^2 - 4ac}}{2a} \tag{2.49}$$

$$a = \frac{1}{3}(1 + cos\theta)^2(2 - cos\theta)(\rho_L - \rho_G)g \tag{2.50}$$

$$b = \frac{1}{2}(\pi - \theta + cos\alpha sin\theta)\rho_L v_L^2 C_D \tag{2.51}$$

$$c = -2sin\theta\sigma \frac{\pi(\alpha - \beta)}{\pi^2 - (\alpha - \beta)^2}(sin\alpha + sin\beta) \tag{2.52}$$

The following values have been used for calculating the detachment radius. For the density and viscosity of the electrolytes, the concentrations are assumed to be 25wt% and 33wt% for NaCl and NaOH, respectively. All variables are tabulated at 25°C. Since the literature on contact angles is scarce and its difficulty to experimentally measure it, alternatives are required. For the contact angle on the DSA electrode, a value of 38° is used. This is the contact angle on a horizontal RuO_2 electrode [85]. Obviously, the orientation of the electrode might have a significant effect on the contact angle. However, due to lack of better literature, this value will be used. For the contact angle on the Ni electrode, a value of of 43° will be used. This is the contact angle on a vertical Pt electrode [82]. Since no information on Ni electrodes was found, this value will be used. Due to the lack of available literature on values of $\Delta\theta$, the value for oxygen and hydrogen in 20 wt% KOH is used for both NaOH and NaCl [82].

Variable	value
ρ_{NaOH} (kg/m^3)	1356
ρ_{NaCl} (kg/m^3)	1186
ρ_{H_2} (kg/m^3)	0.0824
ρ_{Cl_2} (kg/m^3)	2.900
μ_{NaOH} (Pa s)	$1.39 \cdot 10^{-2}$
μ_{NaCl} (Pa s)	$1.68 \cdot 10^{-3}$
σ_{NaOH} (N/m) [38]	$9.00 \cdot 10^{-2}$
σ_{NaCl} (N/m) [38]	$8.26 \cdot 10^{-2}$
θ_{H_2} (°) [82]	43
θ_{Cl_2} (°) [85]	38
$\Delta\theta_{H_2}$ (°) [82]	1.5
$\Delta\theta_{Cl_2}$ (°) [82]	1.5

Table 2.4: Physical properties used for predicting detachment radius on electrodes.

A similar analysis can be performed for bubbles growing on the membrane. This allows for estimating the detachment radius of bubbles when they would grow on the membrane. For Nafion 117, only contact angles with water on a horizontally positioned membrane are available in literature [86]. An additional limitation is the fact that these contact angles are only reported for dry Nafion 117 membranes. As water gets absorbed over time, this might affect the contact angle [87]. Nevertheless, due to the lack of better alternatives, a contact angle of 105° is used. Since no literature was found on the difference between the advancing and receding angle on a Nafion membrane, a value of 1.5°is used for $\Delta\theta$, which is the same value as in the section above.

Variable	value
θ_{H_2} (°) [86]	105
θ_{Cl_2} (°) [86]	105
$\Delta\theta_{H_2}$ (°) [82]	1.5
$\Delta\theta_{Cl_2}$ (°) [82]	1.5

Table 2.5: Physical properties used for predicting detachment radius on Nafion 117 membrane.

For this research a constant mass flow rate of 4 g/s for both electrolytes will be used, which equals a superficial velocity of 0.60 mm/s and 0.69 mm/s for the catholyte and anolyte, respectively. With this, the theoretical detachment radius of a freely growing bubble on a vertical electrode or membrane can be calculated. For bubbles growing on a vertical electrode, a theoretical detachment radius of 0.211 mm is found for chlorine bubbles and a theoretical detachment radius of 0.230 mm is found for hydrogen bubbles. Similarly, this calculation can be performed for bubbles growing on a membrane. Using the same superficial velocity, a detachment radius of 0.564 and 0.603 mm is found for chlorine and hydrogen bubbles, respectively.

3. Methodology

In order to gain insight in the effects of bubble behaviour on the cell performance, multiple measuring techniques were used. Their results were combined in order to draw conclusions. To perform those measurements, a pilot-scale electrolyzer was used. The employed techniques are explained in the upcoming sections.

3.1 Electrochemical cell

A custom zero-gap electrochemical reactor capable of reaching chlorine production rates up to 1.2 L/min (at 10 kA/m^2) was used. The electrolyzer consisted of two compartments separated by a cationic exchange membrane (CEM). A Gylon 3504 sealing plate from Eriks was used to expose 150 cm^2 (50 x 3 cm) of the membrane. The anodic compartment was filled with acidic brine solution and the cathodic compartment with sodium hydroxide. The electrolytes flowed from the bottom to the top of the cell. A DSA electrode with an Ir/Ru mixed metal oxide (MMO) catalyst coating on Ti with a 50/50 ratio of Ir/Ru was used as anode. The cathode was a Nickel (Ni 200) electrode. Both electrodes had an expanded mesh structure and an geometrical area of 150 cm^2 (50 cm x 3 cm). The length x width of the openings was 9 x 3 and 4 x 2 mm for the anode and cathode, respectively. These electrodes were attached with clamps to ensure a proper zero-gap configuration was maintained during operation. Both electrodes were connected to the power supply at 20 points (10 on the left and 10 on the right) in order to distribute the current as evenly as possible. The housing of the reactor was made from titanium and nickel metal for the anode and cathode side, respectively. Titanium was used for the anodic side for its resistance to chlorine and hydrochloric acid. Nickel was used on the cathodic side for its resistance to concentrated NaOH solutions. The cell contained windows, which allowed for visual assessment of the cell during operation. The custom electrochemical cell was able to withstand pressures of up to 50 bar and temperatures of 90 °C. However, it was only used at atmospheric conditions due to limitations of the rest of the set-up.

Figure 3.1: The custom zero-gap electrolyzer with inlet and outlet closed. The wires on the side are to connect the power supply to the electrodes.

3.2 Experimental set-up

The experimental set-up for the chlor-alkali membrane electrolysis had two separate circuits, the anolyte and catholyte circuit. The catholyte circuit only consisted of the electrolyte vessel containing a NaOH solution. The anolyte circuit was more complicated, it included an electrolyte vessel containing brine, gas-liquid separator, gas chromatograph, scrubbers and acid addition. A simplified overview of the set-up is shown in figure 3.2. A more detailed version of the P&ID of the system can be found in Appendix E.

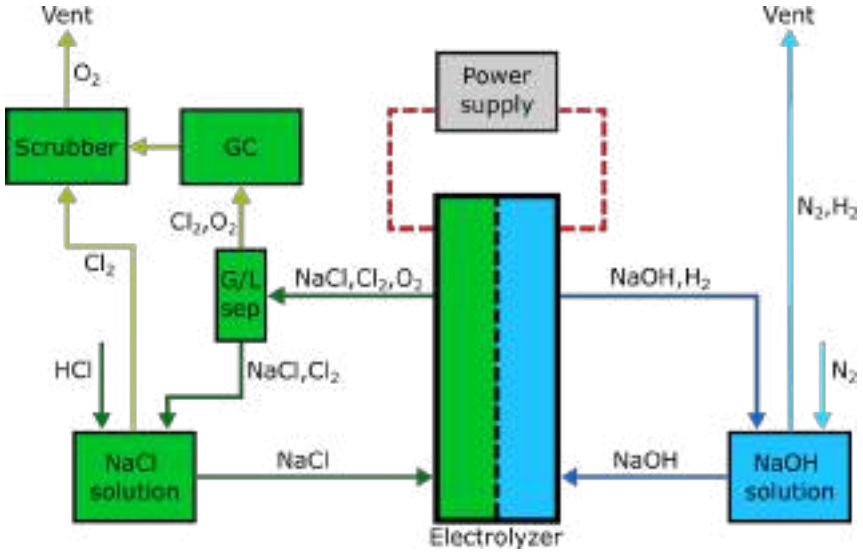

Figure 3.2: Overview of the experimental set-up used for chlor-alkali membrane electrolysis.

Electrolytes

The anolyte was prepared as a 25 wt% solution by dissolving NaCl ($\geq$ 99.9% purity) from VWR Life Science in distilled water ($\geq$15 MΩ·cm). It was acidified to a pH of 2 with 1 M (0.995-1.005 M) HCl from Merck TitriPUR®. For the catholyte a 32.0-33.0 wt% (>99.4% purity) NaOH stock solution from Merck was used. During operation the concentrations changed due to the production of NaOH and consumption of NaCl.

Electrolyte vessels

Glass electrolyte vessels with a volume of 5 L were used to store the electrolytes. To ensure good mixing of the electrolytes, magnetic stirring was used. During operation the overhead of the catholyte vessel was continuously flushed with nitrogen to remove the produced hydrogen. The anolyte vessel was not flushed with nitrogen during operation, because diluting the chlorine might have resulted in incomplete conversion of chlorine in the scrubbers, due to mass transfer limitations. The anolyte vessel was flushed with nitrogen after operation to remove the leftover chlorine. Cooling coils were placed inside both vessel to remove the heat produced during operation. To maintain a desired pH, an acid addition system was implemented for the anolyte vessel. Lastly, high and low liquid level sensors as well as thermocouples were attached to the outside of the vessel for safety reasons.

Acid addition

A 1 liter glass vessel was positioned near the anolyte vessel. This vessel contained two tubes at the top. One was positioned above the liquid level and was used to pressurize the vessel up 1.3 bar with nitrogen in order to overcome the pressure inside the anolyte vessel. The other was placed below the liquid level and was used to add 1 M HCl to the anolyte vessel. The addition of HCl was regulated by a valve which opened automatically when the pH got above the set pH value. Feedback was provided by a M300 Process transmitter connected to an InPro4850i/SG/120 pH sensor from Elscolab.

Tubing

Throughout the system PFA tubing was used because of its excellent resistance to the involved chemicals in both circuits. Inside the pump of the anolyte circuit a piece of Viton® tubing was placed, because PFA tubing is not compatible with a peristaltic pump. This piece of tubing does not have excellent resistance to alkali solutions, therefore it was important to acidify the anolyte before circulation.

Heat tracing and thermocouples

Multiple thermocouples were used to accurately monitor the temperature of different streams of the system. The tubes leading to the inlet of the electrolyzer were fitted with heat tracings. Feedback to those heat tracings was provided by thermocouples placed in the same tubes in order to reach the desired inlet temperature. Heat tracers around the tubes towards the GC were used to heat the gas up to 150°C. This was necessary to prevent water condensation from entering the GC.

Pumps

The catholyte circuit used a Gather pump (model: 1MA-J/12/X-SS/Q/DLC/GFK/DS2D50) from Suurmond suitable for temperatures, pressures and flow rates up to 90°C, 40 bar and 0.1-1.5 L/min. Both the body and shaft of the pump were made of stainless steel, with Nickel alloy/PEEK gears and carbon bearings. For the anolyte circuit a Masterflex L/S® 7521-25 peristaltic pump with a Masterflex L/S® Easy-Load® II pump head was used. Since these type of pumps are not compatible with PFA tubing, a piece of Viton tubing was placed inside the peristaltic pump. This piece of tubing was connected to the PFA tubing with hose clamps. Due to the limited pressure resistance from the connection between the Viton and PFA tubing, it was decided to keep the flow rate and pressure at a maximum of 0.3 L/min and 1 bar. Lastly, a Gather pump was used to control the liquid level in the gas-liquid separator. This pump was suitable for temperatures, pressures and flow rates up to 90°C, 10 bar and 1.5 L/min, respectively. The pump had a titanium body and a shaft with PEEK/PEEK (30% CFK) gears and carbon bearings.

Valves

Solenoid valves from Burkert were used to change the flow into the desired direction. The body of the valves was made of PTFE and could withstand temperatures up to 90°C. The sealing material

of the valves in the catholyte circuit was EPDM, whereas the sealing material in the anolyte circuit was PTFE.

Gas-liquid separator
A 0.5 liter gas-liquid separator was incorporated after the outlet of the anodic reactor compartment. This vessel was tilted at an angle of 45°and had two outlets. One gas outlet connected to the GC and one liquid outlet connected to the anolyte circuit. The vessel had a higher liquid sensor to prevent liquid entering the GC and a lower liquid sensor to prevent the gas-liquid separator pump from running dry.

Gas Chromatograph
An inline TRACE™1300 gas chromatograph from Thermo Scientific with Hastelloy tubing was connected to the gas outlet of the gas-liquid separator and was used to measure the selectivity towards chlorine. The GC could either be included or excluded from the circuit by switching a valve.

Cooling coils
Cooling coils were placed inside both electrolyte vessels in order to remove the heat generated during operation. Both coils were connected to their own Lauda WK 1200 cooler. Both coolers had the capacity to remove 1.2 kW of heat. Water was used as the coolant.

Gas coolers
Both electrolyte vessels were connected to gas coolers at the top to prevent excessive water loss due to evaporation. At the catholyte side, the cooled hydrogen / nitrogen mixture was directly vented via the ventilation point. The cooled chlorine was directed towards the scrubbers to remove the chlorine before it was vented via a ventilation point. Both gas coolers were connected to the same Lauda MT (M3) cooler, with water as a coolant.

Scrubbers
Since chlorine cannot be directly vented into the atmosphere, scrubbers filled with NaOH solution were used in order to convert chlorine to NaOCl and NaCl. Four glass vessels were connected in series. The first vessel (2 L) was connected to the outlet of the gas cooler on the anolyte side and was empty in order to prevent suck back of NaOH directly into the anolyte vessel. The second (2 L) and third vessel (1 L) were filled with 50 wt% NaOH solution (technical grade) from VWR Chemicals. The final vessel (0.5 L) was filled with water and was used as a water lock.

Mass flow meters
In both circuits a Bronkhorst Cori-Flow™M54 mass flow meter made of Hastelloy-C22 was used to control the flow rate. The mass flow meters gave feedback to the pumps in their respective circuits to reach the set flow rate. They are compatible with temperatures up to 120 °C.

Water vessels
Each circuit had its own 5 liter glass water vessel to rinse the system after operation. The water could either be pumped into the electrolyte vessel or through the electrochemical cell.

Power supply
A GEN8-600-3P400 DC power supply from TDK-Lambda capable of reaching 600 A (8 V) was used to supply direct current across the electrochemical cell. The power supply had 40 wires of which 20 were connected per electrode to achieve an even current distribution. All wires were electrically insulated and contained a current probe that prevented the current through a single wire being higher than the compliance limit of the wire.

3.3 Electrochemical Impedance Spectroscopy

An IVIUM Vertex 10A potentiostat was used to perform Electrochemical Impedance Spectroscopy (EIS). EIS is a powerful technique to gain more insights of an electrochemical system. The analysis is based on the response of the system to an imposed sinusoidal current perturbation [88].

By analyzing the response of the system at different frequencies, information about different contributions to the total cell potential can be obtained. In the high frequency region information about the total ohmic resistance of the cell can be obtained, whereas in the low frequency region information about the charge transfer resistance can be found. The strength of this technique lies within the fact that it allows you to measure the contributions at different current densities. This means that the effect of current density on the ohmic resistance and charge transfer resistance can be extracted from the data. The spectra were recorded at 6 points per decade by superimposing a 10% alternating current (AC) signal over the set direct current (DC) over a frequency range from 20 kHz to 100 mHz. A Nyquist plot was then be made of the obtained EIS data, which allowed for extraction of the ohmic resistance, charge transfer resistance and capacitance of the system by fitting it to an equivalent electrical circuit. It was found that only one semicircle can be observed in the Nyquist plots. Therefore, the data is fitted to the following equivalent electrical circuit. Since an electrode does not behave as an ideal capacitor, a constant phase element is used instead of a capacitor.

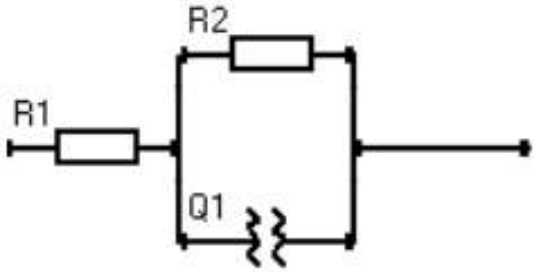

Figure 3.3: Equivalent electrical circuit that is used to fit the EIS data, where R1, R2 and Q1 represent the ohmic resistance, charge transfer resistance and constant phase element.

Information on the Tafel slope and exchange current density could be found by subtracting the measured ohmic resistance and reversible cell potential from the measured total potential.

$$\eta = E_{cell} - E_{rev} - IAR \tag{3.1}$$

The total overpotential was then plotted versus the log of current density in order to obtain the Tafel slope as well as the exchange current density.

3.4 Polarization curve

The power supply was used for polarization curve analysis by setting a certain DC and measuring the corresponding cell potential. The current was applied for five minutes so the system has a sufficient amount of time to equilibrate. The first three minutes are used as an equilibriation time and the average potential over the last two minutes is taken as the potential corresponding to the set current. The data points are then plotted in a polarization curve and fitted to the following equation.

$$E_{cell} = E_{rev} + b\ log\left(\frac{I}{I_0}\right) + IAR \tag{3.2}$$

Where the reversible potential is concentration and temperature dependent and is calculated according to the equations proposed in section 2.1.1. This means that b, I_0 and AR are the parameters that are being fitted simultaneously. It should noted that via this technique only a combined Tafel slope and exchange current density can be fitted, and no conclusions on the individual half reactions can be drawn. The combined Tafel slope is used in order to reduce the number of fitting parameters [27]. These combined Tafel slope and exchange current density can be derived as follows.

$$\eta_A + \eta_C = b_A\ log\left(\frac{I}{I_{0,A}}\right) + b_C\ log\left(\frac{I}{I_{0,C}}\right) = b_{tot}\ log\left(\frac{I}{I_{0,tot}}\right) \tag{3.3}$$

Where the combined Tafel slope and exchange current density are defined according to the following expressions.

$$b_{tot} = b_A + b_C \quad \text{and} \quad I_{0,tot} = I_{0,A}^{b_A/b_{tot}} \cdot I_{0,C}^{b_C/b_{tot}} \tag{3.4}$$

Another limitation is the fact that all the fitted parameters are averaged over the applied current density range, even though they might be current density dependent.

3.5 Video analysis

A Dino-Lite USB microscope, 1280x960 pixel, 30 fps and 10-50x magnification was positioned in front of the electrolyzer on either side. Because a transparent Nafion 117 membrane was used, the electrode surface facing the membrane of the electrode on the opposite side of the Dino-Lite microscope could be visualized. Front and back lighting was used to improve visibility. From these videos, the bubble behavior inside the gap could be explored. It was more difficult to obtain clear videos during operation at higher current density, due to the large amount of bubbles present in the bulk of the electrolyte, reducing the visibility. Due to time constraints, no image analysis was performed, which means these results are purely quantitative. Another thing that should be taken into account is the fact that these analyses were performed at the bottom window of the cell (see Figure 3.1), meaning that only a small fraction of the electrode is analyzed and thus local behavior is observed. The position of the microscope was altered in front of this bottom window to obtain a better understanding about how bubble behavior changes with position. Even though different positions were analyzed, it should be realized that the behavior at the top of the electrolyzer might be different as compared to the bottom.

4. Results and Discussion

Fundamental questions such as 'do bubbles affect the cell potential in a zero-gap configuration?' and 'on which side of the electrode is the reaction taking place in a zero-gap configuration?' are still either unanswered or highly debated. Therefore, an attempt will be made to answer them. Video analysis will be used in order to gain insights in the bubble behavior inside a zero gap configuration and compared with polarization curves in order to conclude whether the visual observations make sense with the electrochemical performance of the cell. Since it remains rather difficult to (in)directly quantify the electrode coverage, gas holdup inside the gap as well as the membrane coverage, these parameters will not be measured. Between days the the setup was broken down and rebuild. This results in videos being taken at different positions with different lighting. This should be considered as an advantage rather than a disadvantage, since locally different behavior is observed. All videos are taken at a temperature of 28°C and a mass flow rate of 4 g/s for both electrolytes, unless stated otherwise. All videos are made at the bottom of the electrochemical cell, to reduce the visual hindrance of rising bubbles. This means that careful note should be taken when generalizing the observed behavior for the entire cell. The side of the electrodes facing the membrane will be referred to as the **frontside** and the sides of the electrodes facing the bulk will be referred to as the **backside**. Since it is difficult to depict the observed bubble behavior, videos are attached to this report. The name of the video is reported at the beginning of its corresponding section. Due to the different magnifications used for each picture, a length scale is added to all pictures.

4.1 Video analysis

4.1.1 Cathode

Bubble curtain between electrode and membrane
In Figure 4.1 and the videos 'bubble curtain (I = 6.7)', 'bubble curtain (I = 33.3)' and 'bubble curtain (I = 66.7)' one can see a bubble curtain between the cathode and membrane at 6.7 and 33.3 mA/cm^2 and a bubble froth between the cathode and membrane at 66.7 mA/cm^2.

As mentioned in Section 1.2, in a zero-gap configuration, bubbles should ideally be transported towards the bulk of the electrolyte via the openings in the electrodes. However it is found that bubbles also remain between the electrode and membrane. A curtain of hydrogen bubbles is observed between the cathode and the membrane. When focusing on bubbles that are stuck to the membrane, it can be seen that the bubble curtain moves behind these bubbles, indicating that this curtain is indeed located between the electrode and the membrane. When increasing the current density from 6.7 mA/cm^2 to 33.3 mA/cm^2, the bubble curtain is still observed, however the total gas volume seems to increase and larger bubbles are seen. When increasing the current density even further (67.7 mA/cm^2), a significantly different behavior is observed. Instead of small hydrogen bubbles flowing upwards, a stagnant bubble froth is observed. The froth seems to originate from the fact that some larger bubbles block the pathways of the other bubbles, which hinders them from rising. The bubbles then start to accumulate and coalesce until the froth is formed. Sometimes part of the froth gets released when a pathway is opened. However, after some time the pathway gets blocked again with bubbles, causing the froth to start growing again.

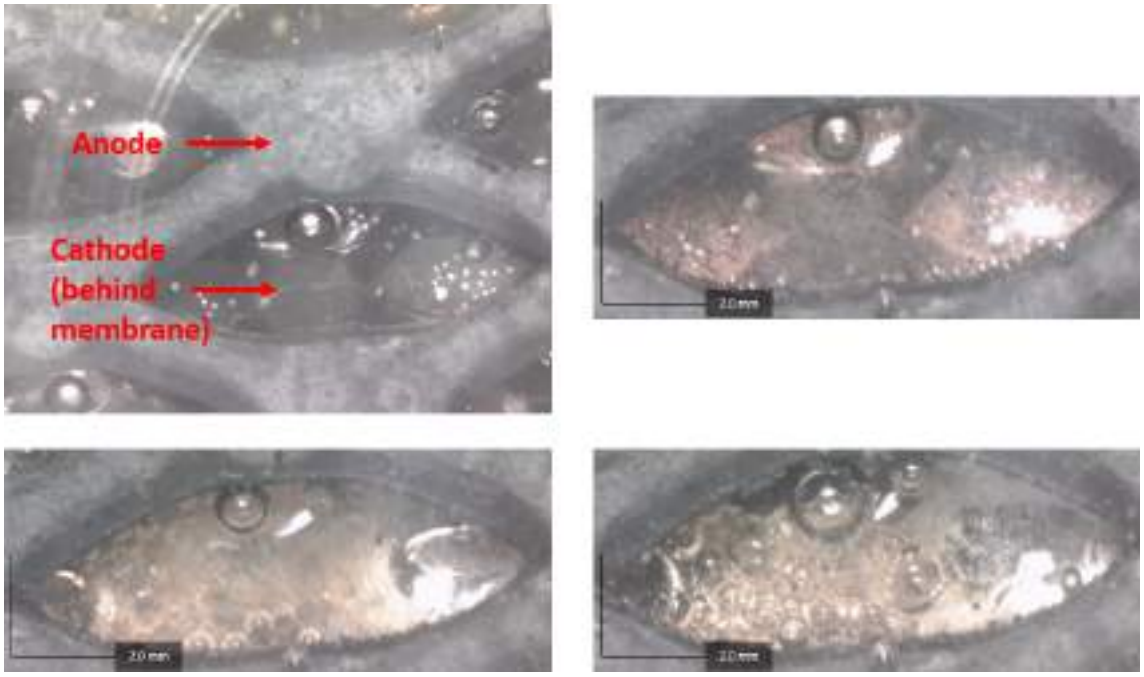

Figure 4.1: View of electrochemical cell during operation. Front electrode is anode and back electrode is cathode. In between the electrodes there is a Nafion 117 membrane. The bubble behavior is visualized at different current densities; 0, 6.7, 33.3 and 66.7 mA/cm^2 for top left, top right, bottom left and bottom right, respectively.

Static bubbles in the gap

In top sub figure of Figure 4.2 and the video 'small bubbles in gap', one can see small bubbles between the cathode and membrane with a diameter between 0.2 and 0.3 mm before they are pushed towards the openings of the electrode. In bottom sub figure of Figure 4.2 and the video 'large bubbles in gap', one can see trapped larger bubbles growing. At a certain point these bubbles coalesce and eventually the bubble is released by buoyancy. After the removal of the bubble, a new bubble grows at exactly the same position. In the videos 'rising bubble gets trapped 1' and 'rising bubble gets trapped 2' one can see a rising bubble getting trapped at a similar position. Due to the long interval between these occurrences, two separate videos are added.

At some positions larger bubbles nucleate inside the gap. These static bubbles are seen to be removed via multiple mechanisms. Sometimes these bubbles coalesce with neighbouring static bubbles forming relatively large films until they are either released by buoyancy or coalesce with larger bubbles occupying the openings of the cathode as described in section 4.1.1. Sometimes these static bubbles grow up to a diameter of around 0.2 - 0.3 mm, while (seemingly) maintaining their spherical shape. When they reach this size, they are pushed towards the rim of the openings in the cathode, most likely due to capillary forces. This implies that the distance between the cathode and the membrane is around 0.2 - 0.3 mm at certain positions, which is on the large side for a zero-gap configuration, but not unrealistic, especially for a large electrolyzer like the one employed for this research. It is important to realize that this distance can differ along the cell and thus that the gap size is not a constant. Sometimes static bubbles reaching diameters of 0.7 - 0.8 mm are observed, however it seems like the bubbles reaching this size are not spherical anymore.

Generally, these bubbles grow at the same location, indicating that there are preferred nucleation sites. Sometimes the static bubbles do not nucleate at a certain position, but a rising bubble gets trapped. The main difference between the nucleating bubbles and the trapped bubbles, is the fact that the trapped bubbles do not get removed by buoyancy, but only by coalescing with the large bubbles in the openings. Just like the nucleating bubbles, the rising bubbles get stuck at the same position. One possible explanation for this phenomenon is the fact that the membrane

has some hydrophobic spots or imperfections, causing the bubble to attach at these positions. Another explanation could be that there is a local minimum distance between the electrode and the membrane, due to the 3D structure of the electrode, causing a rising bubble to get trapped.

Figure 4.2: Front electrode is anode and back electrode is cathode. Static bubbles reaching a diameter of around 0.2 - 0.3 mm during operation at a current density of 6.7 mA/cm^2 (top) and static bubbles reaching a diameter of around 0.7 - 0.8 mm at a current density of 300 mA/cm^2 (bottom). Both pictures are taken at different positions of the electrode.

Sliding bubbles and films in the gap

In the top sub figure of Figure 4.3 and the video 'sliding bubbles in gap', one can see bubbles sliding along the cathode surface between the cathode and membrane. In the bottom sub figure of Figure 4.3 and the video 'sliding films in gap', one can see gas films sliding along the cathode surface between the cathode and membrane.

Besides static bubbles, mobile bubbles sliding along the electrode surface are also observed. This phenomenon occurs at a similar current density as the bubble froth, which is around 66.7 mA/cm^2. At lower current densities, a bubble curtain is observed. The bubbles are generated on the electrode surface and pushed towards the openings of the cathode where they form larger bubbles on the rim. An interesting observation is the fact that the sliding bubbles seem to occur at positions where the cathode and anode are aligned with each other. At positions where the cathode is facing an opening of the anode, this behavior is not observed. This could possibly be explained by the fact that the gap between the cathode and membrane is narrower when the cathode is aligned with the anode instead of an opening. Similar behavior is observed elsewhere, however instead of spherical bubbles, flatter bubbles / gas films sliding towards the rims of the cathode are observed. Contrary to the

sliding bubbles, the sliding films are observed at positions where the cathode is facing an opening instead of being aligned with the anode. Since these films seem rather flat and are able to occur at positions of the cathode facing an opening of the anode, it seems like a closer to perfect zero-gap is achieved at this position as compared to the position where the sliding bubbles are observed.

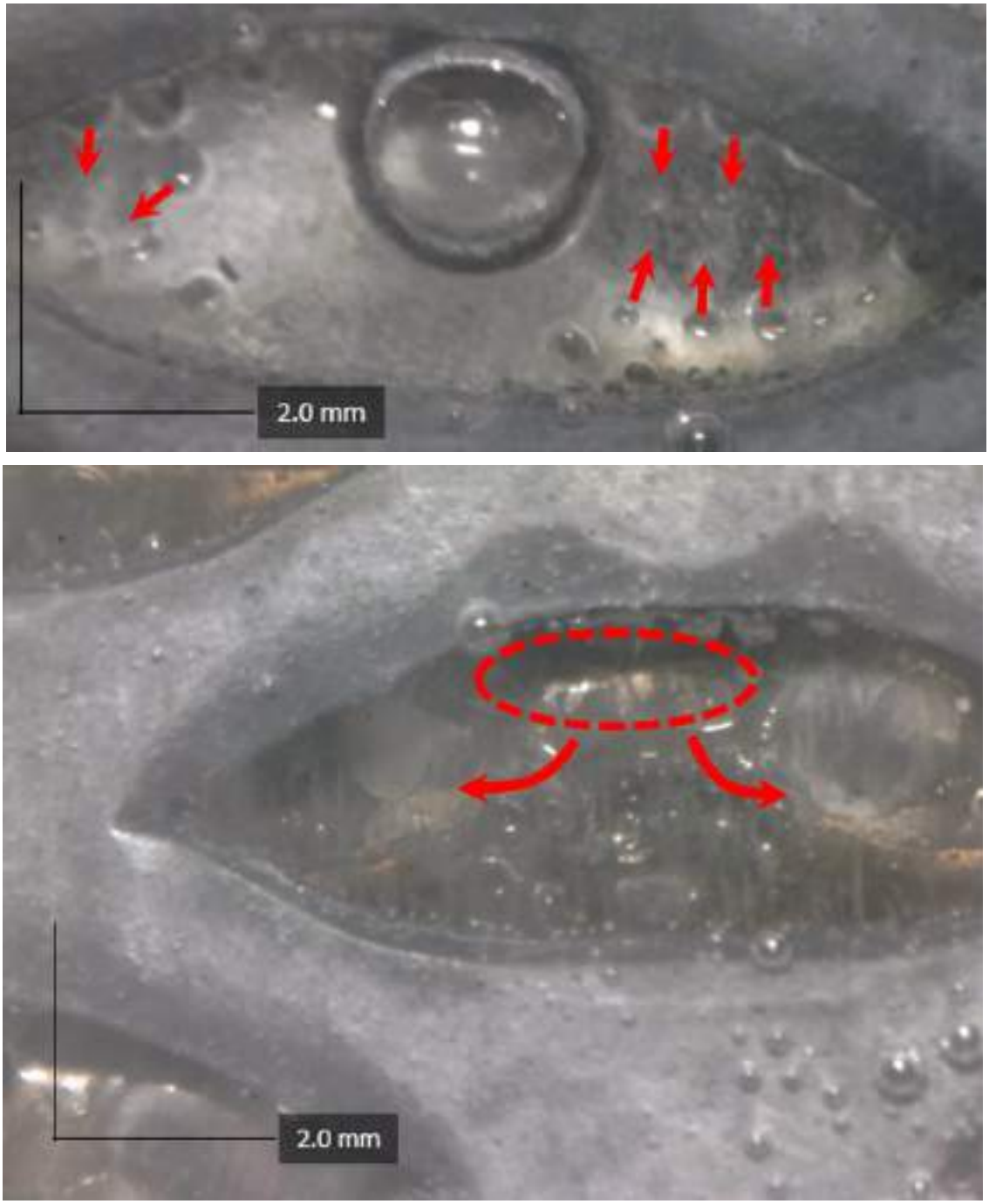

Figure 4.3: Front electrode is anode and back electrode is cathode. The different behavior is observed at different positions of the electrode at a current density of 66.7 mA/cm^2. The arrows indicate the sliding direction of the bubbles and films.

Large bubbles occupying cathode openings

In the bottom sub figure of Figure 4.4 and the video 'large bubbles', one can see the large hydrogen bubbles generated at the cathode. In the figure of Figure 4.5 and the videos 'gas pocket (seen from

anode)' and 'gas pocket (seen from cathode)', one can see gas pockets left behind after detachment of the large hydrogen bubbles.

At the rims of the cathode, larger bubbles are being formed due to the continuous flux of sliding bubbles and films as mentioned in the previous subsection. Some of these bubbles detach relatively early, around a diameter of 0.4 to 0.7 mm. However, some of these bubbles remain attached and grow by coalescence until most of the opening is occupied by the bubble, reaching diameters above 3 mm. These bubbles can remain stuck after operation, even if the system is flushed with a superficial electrolyte velocity of 1 mm/sec.

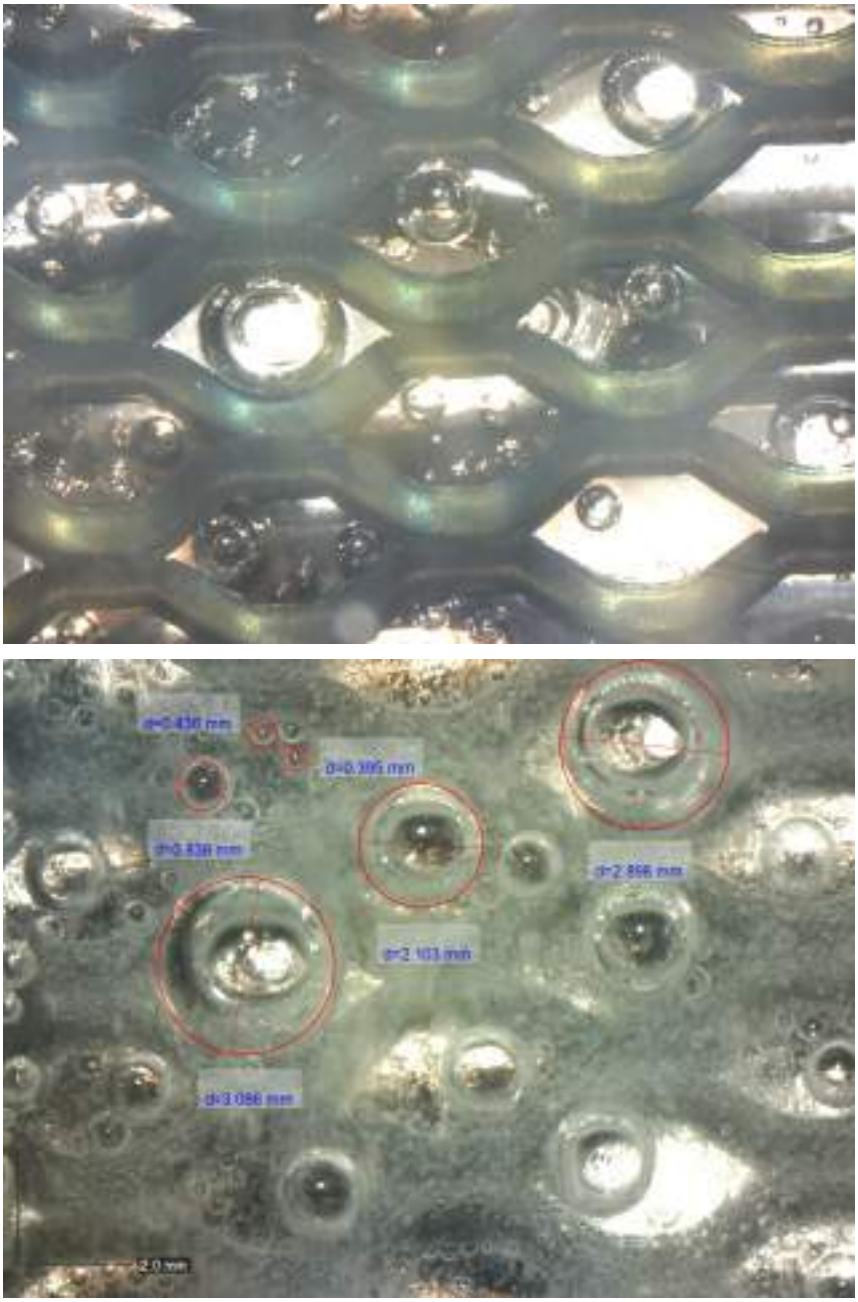

Figure 4.4: Front electrode is cathode and back electrode is anode. The medium sized bubbles (0.4 - 0.7 mm diameter) and the large bubbles (>3 mm diameter) are shown at a current density of 66.7 mA/cm^2 (bottom). A picture of the electrode after operation is added for reference (top).

Assuming the large bubbles are only attached to the membrane, a theoretical detachment diameter of 1.206 mm is predicted, which is smaller than the experimentally observed bubbles. Firstly, the contact angle and deviation between the advancing and receding angle might be significantly different in reality compared to the values used for the prediction. However, due to the lack of available literature, alternatives were required. Secondly, the drag acting on the bubble is less in reality as compared to the prediction. This is due to the fact that part of the bubble is inside the gap (where the flow rate might be lower) and part of it is above the electrode, which also blocks some of the cross sectional area experiencing drag (see Figure 4.6). Lastly, additional forces might be present for this type of bubbles, since they might also be attached to parts of the electrode.

When positioning two Dino-Lite microscopes oppositely to each other at the exact same position, an interesting observation about the large bubbles was made. These large bubbles often leave a gas pocket behind after detachment. This gas pocket is partially trapped between the electrode and the membrane and allows a new large bubble to grow.

Figure 4.5: Gas pocket left behind by large bubble after detachment seen from anode (top) and seen from cathode (bottom)

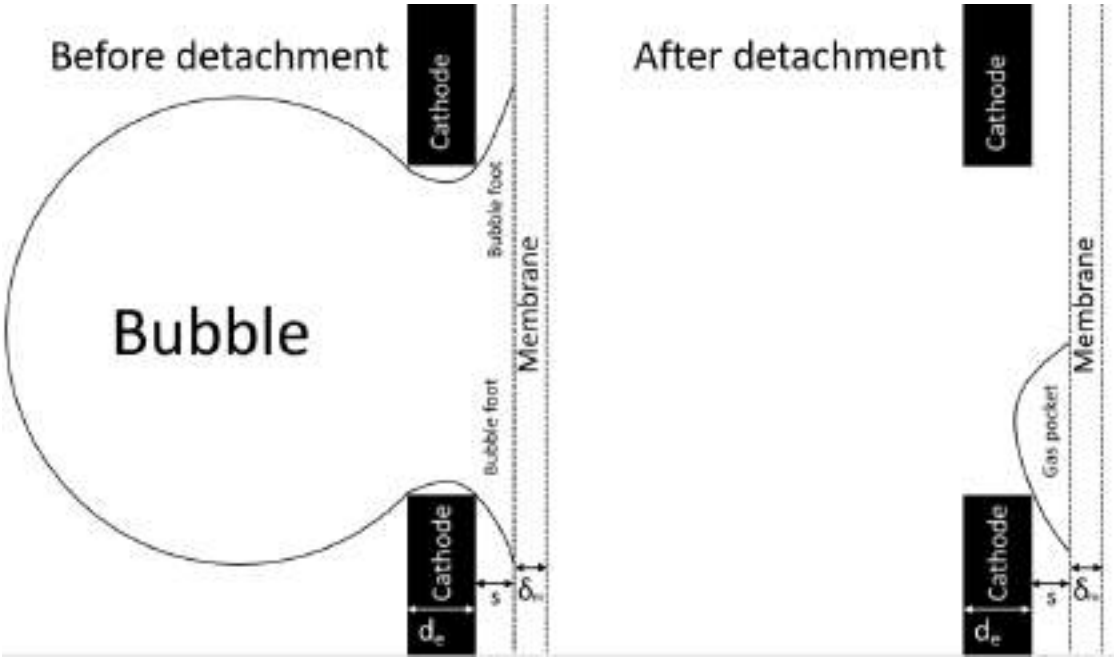

Figure 4.6: Schematic side view of the gas pocket left behind after detachment of a large bubble, where δ_m, s and d_e are approximately 190, 250 and 400 μm, respectively.

According to literature, the bubble effects on the cathodic side of the chlor-alkali process are more pronounced as compared to the anodic side [89]. According to equation 2.41, the tension force increases with increasing surface tension of the electrolyte. A higher surface tension, will consequently result in a larger detachment radius. Since the catholyte has a higher surface tension than the anolyte, this could be a reason why bubble effects are more pronounced at the cathodic side. This is in line with the experimental observations. The hydrogen bubbles are generally able to reach a larger size in combination with the fact that gas pockets remain after detachment, whereas this behavior is not observed for the chlorine bubbles.

Active side

In Figure 4.7 and the video 'cathode backside active', one can see the backside of the cathode becoming active after 10 seconds of switching on the current. The video starts at the moment the current is switched on.

As described by all the phenomena above, the frontside of the cathode is active, since gas bubbles are nucleating and growing inside the gap. However, when looking at the backside of the cathode, it is also active. When starting operation, a lot of small bubbles are starting to grow at the backside. Interestingly, the bubbles only start to grow at the backside after about 10 seconds of switching on the current at a current density of 6.7 mA/cm^2. One possible explanation could be that initially the current flows via the frontside of the electrode, but whenever gas starts to buildup inside the gap, the current will start to also flow via the backside of the electrode due to the increase in resistance of the initial pathway. Another explanation could be that it takes more time to reach the required supersaturation to initiate bubble nucleation at the backside of the electrode.

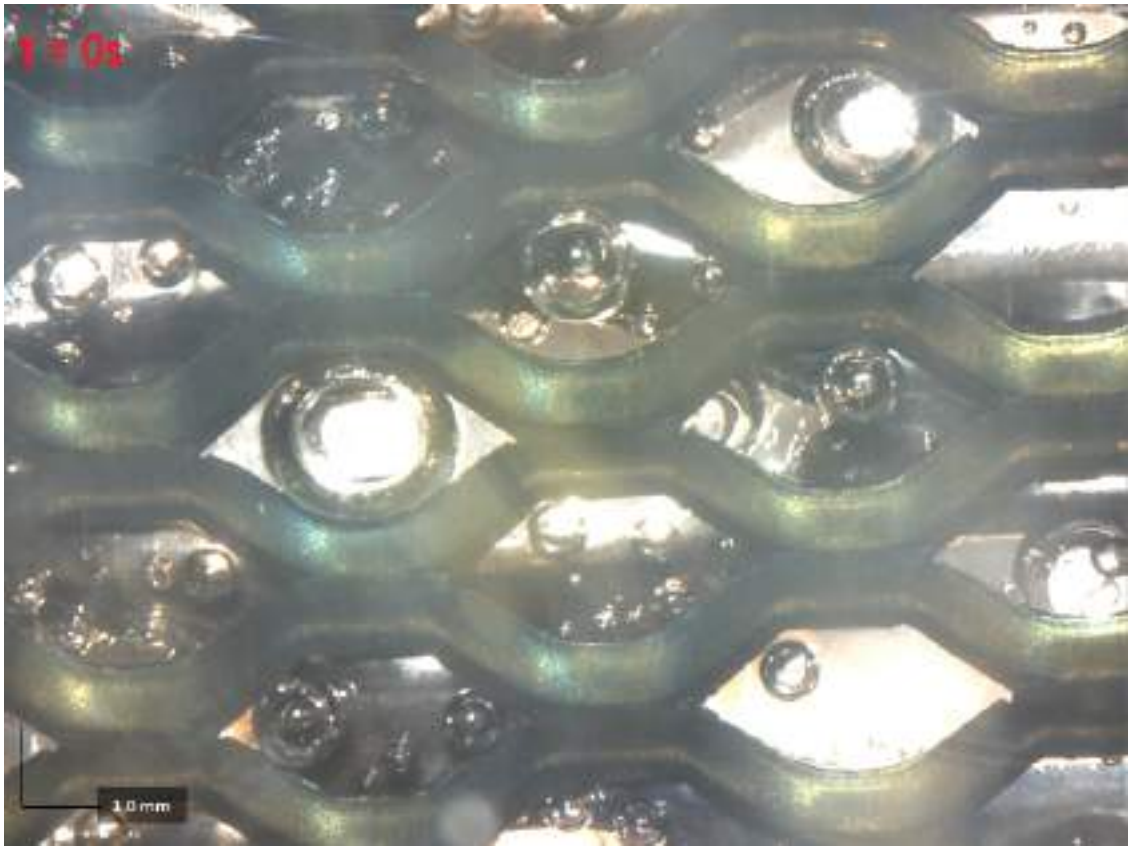
t = 0s
1.0 mm

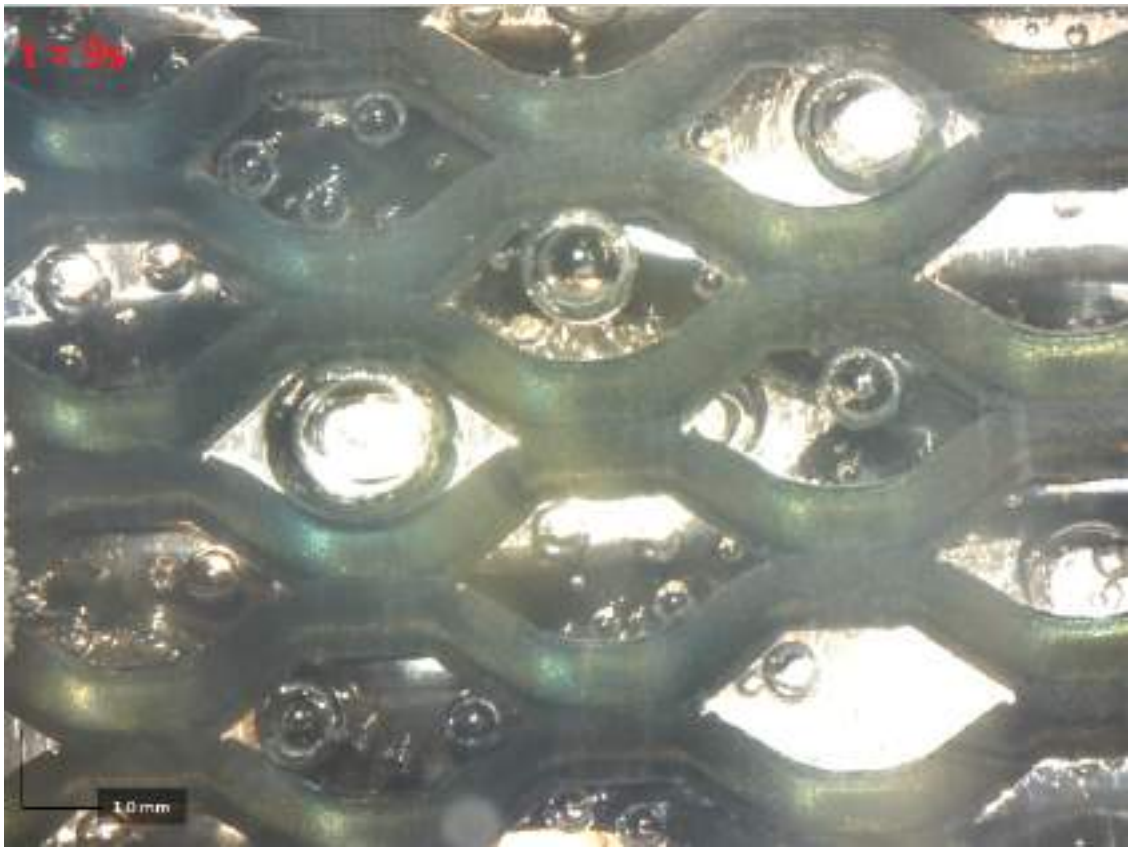
t = 9s
1.0 mm

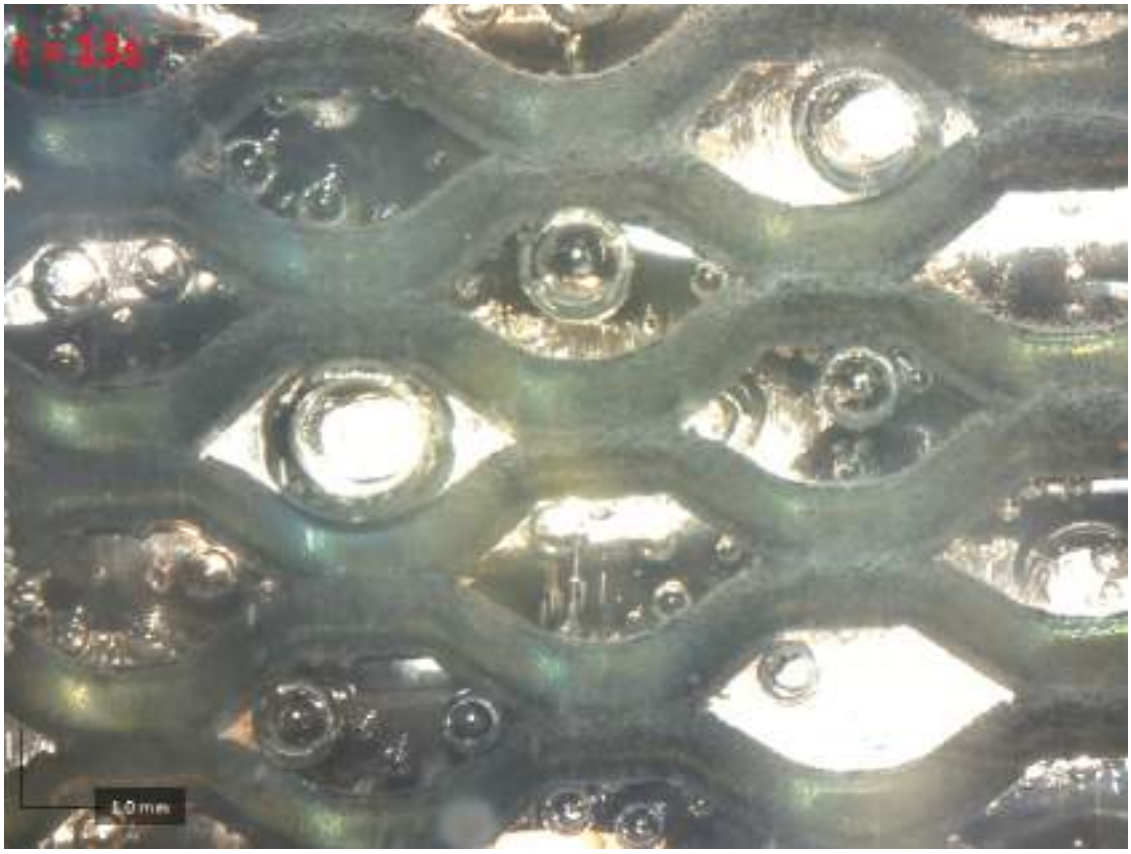
t = 13s
1.0 mm

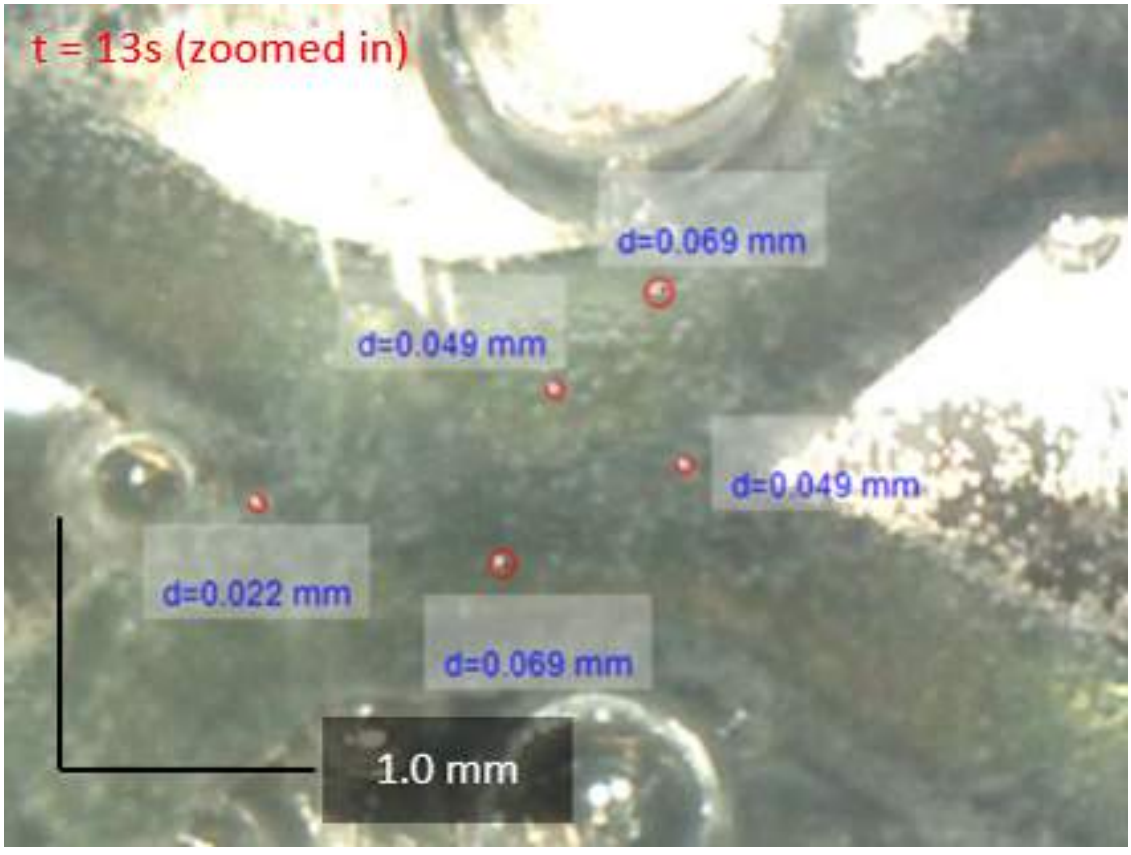
t = 13s (zoomed in)
d=0.069 mm
d=0.049 mm
d=0.049 mm
d=0.022 mm
d=0.069 mm
1.0 mm

Figure 4.7: Front electrode is cathode and back electrode is anode. The backside of the cathode over time where t = 0s indicates the moment the current is switched on at a current density of 6.7 mA/cm^2. Pictures are taken at 0, 9, 13 and 29 seconds after switching on the current from top to bottom. A bubble size measurement is included at 13 seconds.

The bubbles released at the backside of the cathode are small. The measured detachment diameter is between 0.02 and 0.1 mm, however it seems like even smaller bubbles are present, which could not be measured due to resolution limitations. These diameters are significantly smaller than the predicted detachment diameter, which is 0.459 mm for a freely growing bubble. This discrepancy can most likely explained by the inaccurate value for the contact angle of the bubble with the electrode, since the reported value is for a Platinum electrode, while a Nickel electrode is used for this research. Additionally, Vervaecke showed experimentally that the contact angle of a hydrogen bubble on a vertical Nickel electrode is closer to 10° rather than 43°. When a contact angle of 10° is used, the theoretical detachment diameter is 0.114 mm, which is much more in line with the experimental observed diameters.

4.1.2 Anode

Since the solubility of chlorine is relatively high, few bubbles are being generated, especially at lower current density. The difference in electrode structure; larger openings for the anode and smaller openings for the cathode, makes it also more difficult to observe the anodic gap when looking from the cathodic side. This results in less observations being made for the anode as compared to the cathode.

Bubble appearing from inside the gap
In Figure 4.8 and the video 'bubble appearing anode', one can see the sudden appearance of a bubble at the anodic side that was initially trapped between the anode and membrane.

When observing the backside of the anode, sometimes bubbles appear suddenly from the frontside of the electrode. This is most likely due to the bubbles between the anode and the membrane being pushed towards the openings by capillary forces. At the rim these bubbles grow, seemingly due to

coalescence of bubbles generated at the frontside. This is similar to the behavior of the bubbles at the rim of the cathode growing due to coalescence of the sliding bubbles / films. Considering the size of this bubble, it seems like the distance between the anode and membrane is also significant, since this bubble was able to be trapped between the anode and membrane.

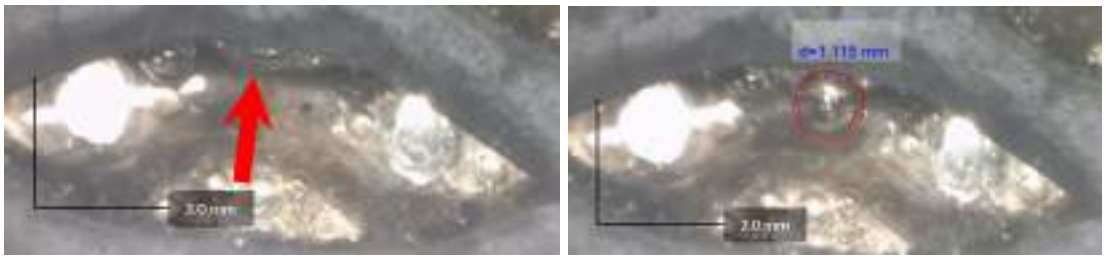

Figure 4.8: Front electrode is anode and back electrode is cathode. One picture is just before the bubble appearing (left) and the other picture is just after the bubble appearing from the front of the electrode. The time between these pictures is less than 0.5 seconds.

Bubbles sliding along rim of the electrode openings
In Figure 4.9 and the video 'bubbles sliding along rim', one can see small bubbles sliding along the rim of the openings at the anode. These bubbles collect at the top where they coalesce and form relatively large bubbles.

Generally, smaller bubbles attached to the rim of the openings on the anode, slide upwards along the rim and coalesce at the top of the opening. Here, larger bubbles are formed until they detach, which typically happens at a diameter between 1.5 and 2.7 mm. This behavior is only observed at higher current densities, since at lower current densities, most of the produced chlorine dissolves in the electrolyte.

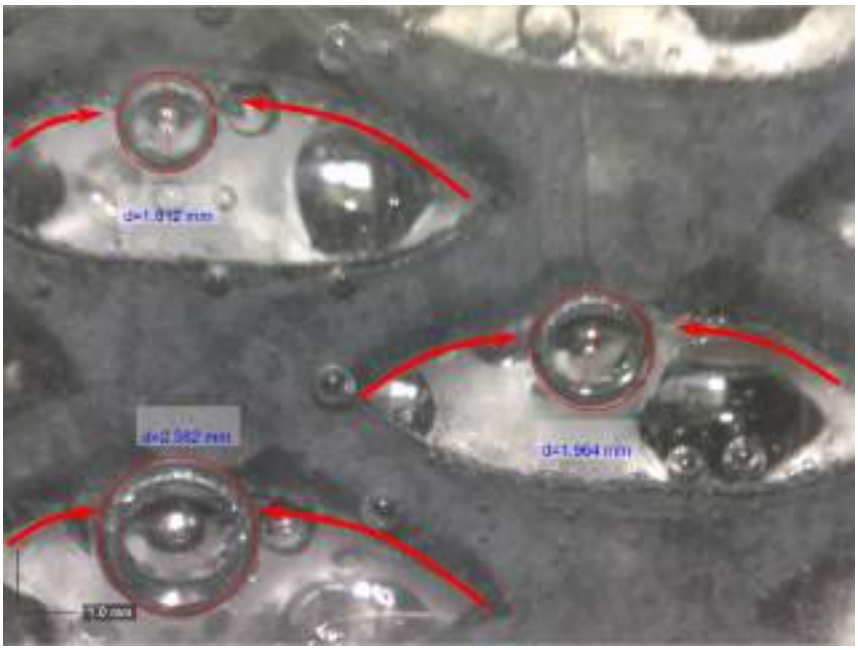

Figure 4.9: Front electrode is anode and back electrode is cathode. The sliding direction of the bubbles is indicated with the arrows and the large bubble formed due to coalescence is indicated with the ring around it.

Small bubbles on backside of anode

In Figure 4.10 and the video 'small bubbles anode', one can see small bubbles growing on the backside of the anode.

At the backside of the anode, small bubbles are nucleating. They generally detach around a diameter between 0.15 and 0.3 mm. According to the force balance, the predicted detachment diameter is around 0.421 mm. This prediction is not that far off from the actual value, however as for the hydrogen bubbles, some inaccuracies in the values for the contact angle and $\Delta\theta$ might be present, which causes the predicted diameter to be slightly off.

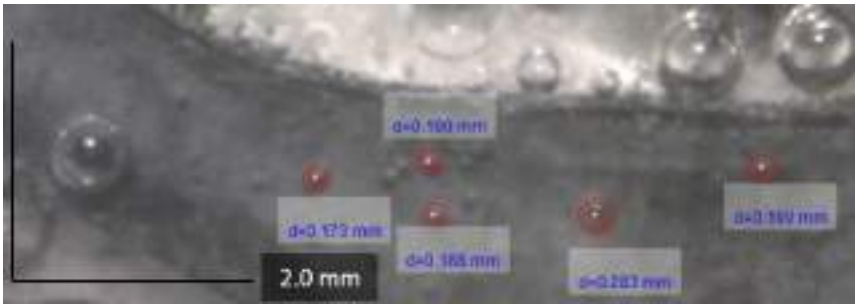

Figure 4.10: Front electrode is anode and back electrode is cathode. Small bubbles growing at the backside of the anode 100 mA/cm^2.

4.2 Electrochemical performance

The performance of the cell can be shown by the polarization curves. The experimentally found polarization curves and their fits according to equation 3.2 are shown in Figure 4.11. The parameters found by fitting are tabulated in Table 4.1. Where E_{rev} is calculated according to the correlations proposed in section 2.1.1, the other parameters are found via fitting. A complete list of experimental conditions can be found in Appendix F.

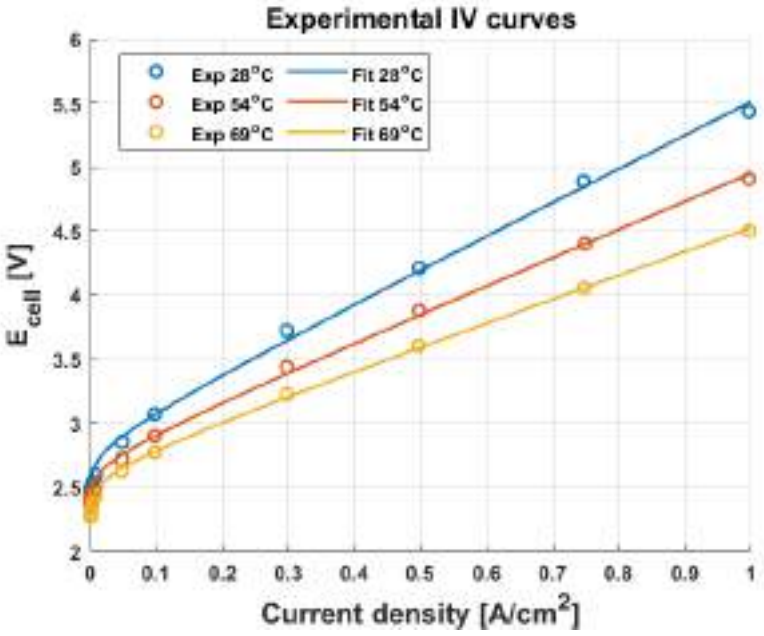

Figure 4.11: Experimental polarization curves obtained with power supply and their fits to the equation $E_{cell} = E_{rev} + b \log(I/I_0) + IAR$ at 28, 54 and 69°C.

Parameter	28°C	54°C	69°C
E_{rev} (V)	2.286	2.250	2.231
b (V/dec)	0.150	0.130	0.140
I_0 (A/cm^2)	$2.74 \cdot 10^{-5}$	$3.90 \cdot 10^{-5}$	$2.09 \cdot 10^{-4}$
AR (Ωcm^2)	2.539	2.131	1.778

Table 4.1: Fitting parameters for curves in Figure 4.11.

The drawback of this type of analysis, is the fact that an average for all the fitted parameters is taken over current density, while it would be interesting to see how they change with current density. In order to be able to see how the ohmic resistance changes with current density, EIS was performed. However, when analyzing the Nyquist plots (see Appendix G.), such as the one shown below, unexpectedly high values were obtained (>10 Ωcm^2). Since relatively large electrode areas are used for this research, the measured resistance will be small. Therefore, small inaccuracies will have a significant effect. It is assumed that cable or contact resistances caused the measured ohmic resistance to be higher than expected.

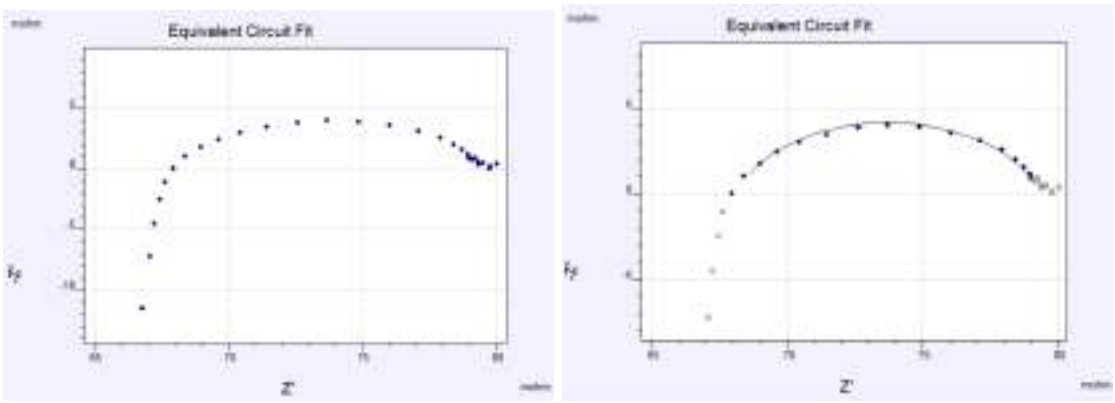

Figure 4.12: Nyquist plot with all the measured data points over the entire frequency range (left) and the fit of the data points (excluding the ones at high and low frequencies) with the equivalent electrical circuit depicted in Figure 3.3 (right). Current density of 50 mA/cm^2, 28°C, mass flow of 4 g/s for both electrolytes.

Therefore, the ohmic resistance values obtained from EIS were deemed to be unsuitable to describe the ohmic resistance of the cell. However, this ohmic resistance could still be used in order to determine the Tafel slope and exchange current density. By correcting the cell potential that is measured with the potentiostat for the ohmic drop, a value for the (combined) Tafel slope and exchange current density can be obtained by plotting the overpotential versus the log of current density.

$$\eta_{tot} = E_{cell} - E_{rev} - IAR \tag{4.1}$$

From the figure below can be seen that the experimentally found data fits nicely to a linear line.

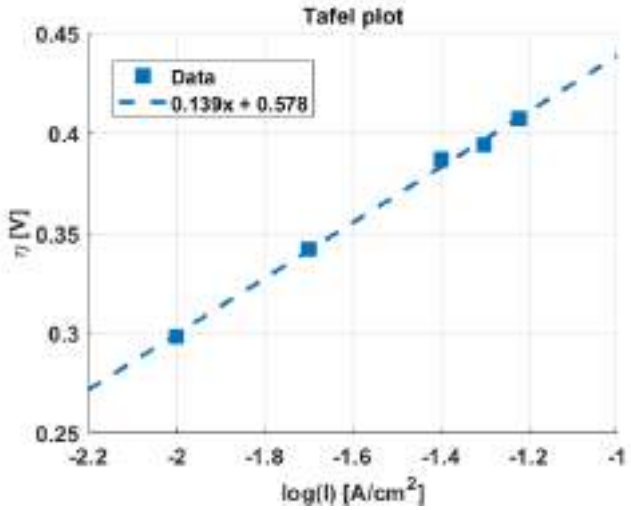

Figure 4.13: Experimental tafel plot with 31.05 wt% NaOH, 16.85 wt% NaCl, 30°C. Total overpotential is found by measuring the cell potential with the potentiostat and correcting it for the ohmic drop and reversible cell potential.

The exchange current density is then obtained by extrapolating the curve to an overpotential of 0V. The following values for the Tafel slope and exchange current density were obtained.

$$b = 0.139 \text{ V} \quad \text{and} \quad I_0 = 7.10 \cdot 10^{-5} \text{ A/cm}^2 \tag{4.2}$$

These values are compared with literature by summing the the lowest CER overpotential and the lowest HER overpotential and similarly with the highest overpotentials (discarding outliers), in order to obtain a spread. For HER only kinetic data on nickel electrodes is used, since a nickel cathode was used for this research. This spread of overpotentials can then be plotted to make a comparison with the experimentally obtained overpotentials as shown in Figure 4.14. For the lower limit the following kinetic parameters are summed: b = 90mV/dec and $I_0 = 10^{-5}$ A/cm^2 + b = 32.7mV/dec and $I_0 = 5.3 \cdot 10^{-3}$ A/cm^2 for HER and CER, respectively [66][61]. For the upper limit the following kinetic parameters are summed: b = 116mV/dec and $I_0 = 7.6 \cdot 10^{-7}$ A/cm^2 + b = 40mV/dec and $I_0 = 1.2 \cdot 10^{-3}$ A/cm^2 for HER and CER, respectively [62][38].

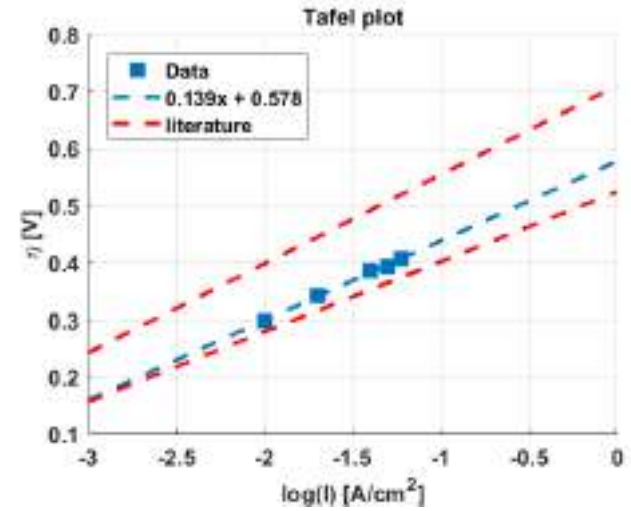

Figure 4.14: Experimentally found combined overpotential compared with overpotentials according to literature. For the lower limit the following kinetic parameters are summed: b = 90mV/dec and $I_0 = 10^{-5}$ A/cm^2 + b = 32.7mV/dec and $I_0 = 5.3 \cdot 10^{-3}$ A/cm^2 for HER and CER, respectively [66][61]. For the upper limit the following kinetic parameters are summed: b = 116mV/dec and $I_0 = 7.6 \cdot 10^{-7}$ A/cm^2 + b = 40mV/dec and $I_0 = 1.2 \cdot 10^{-3}$ A/cm^2 for HER and CER, respectively [62][38].

From this graph can be seen that the experimentally found overpotentials fall within the expected region according to literature. It can also be concluded that the used electrodes perform rather good, since the overpotentials tend to be rather close to the lower end of the spectrum.

In order to obtain the ohmic resistance as a function of current density, the polarization curves were combined with the Tafel slope and exchange current density found with EIS. Instead of directly measuring the ohmic resistance with EIS, it can be calculated by subtracting the reversible cell potential and total overpotential (calculated with Tafel slope and exchange current density found with EIS) from the total cell potential (measured with power supply) and dividing this potential by the corresponding current density. In order to do this, the Tafel slope and exchange current density are assumed to be constant over temperature, concentration as well as current density.

$$IAR = E_{cell} - E_{rev} - \eta_{tot} \tag{4.3}$$

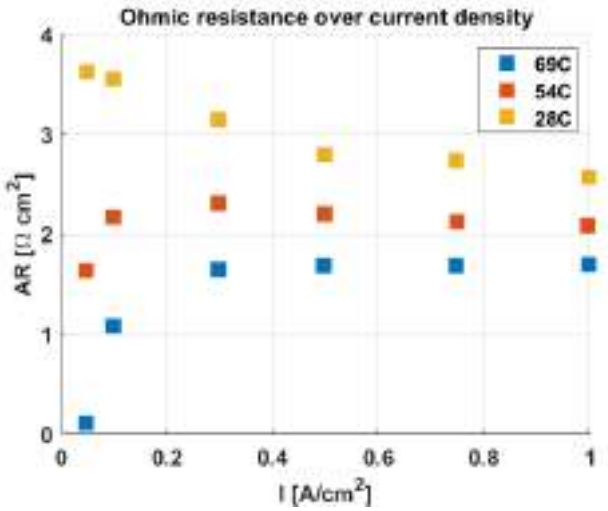

Figure 4.15: Experimentally determined ohmic resistances and membrane resistance according to Sijabat et al at 28, 54 and 69 °C. For complete list of experimental conditions, see Appendix F.

One could argue that the ohmic resistance shows an increasing trend at low current density for the higher temperatures. However, it should be realized that at low current density (<0.2A/cm^2), the activation overpotential is in the same order of magnitude as the ohmic voltage drop. This means that small inaccuracies in the overpotential, could result in significant effects on the calculated ohmic resistance. Since the Tafel slope and exchange current density are assumed to be constant for all conditions, inaccuracies for the activation overpotential might be present. When the slightly inaccurate ohmic voltage drop is then divided by a small current density, the effect of this inaccuracy becomes more pronounced as compared to high current density data points. This can also be observed from the data, since the ohmic resistance approaches zero at low current density at 69°C. Additionally, the fact that the ohmic resistance decreases with current density for the 28°C experiment indicates that some errors are present, since one would not expect the ohmic resistance to decrease with current density. Considering all those factors, it would be a more reasonable conclusion to consider the ohmic resistance to be constant over current density. This conclusion suggest, that the bubble effects play a minor role in the ohmic resistance.

An analysis can be performed in order to evaluate the effect of the gas holdup on the ohmic resistance. When assuming the gap size to be equal to the 0.25 mm that is observed in Section 4.1.1 for both sides and assuming the gas holdup to be constant over current density, the increase in ohmic resistance can be calculated. It should be realized that the gap size can change along the length of the cell and that the 0.25 mm is just a local observation. For this calculation it is also assumed that the gas holdup is equal in both gaps. Looking at the stoichiometry, the same number of moles is produced on both sides, however due to the higher solubility of chlorine, a lower gas holdup might be present in the anodic gap.

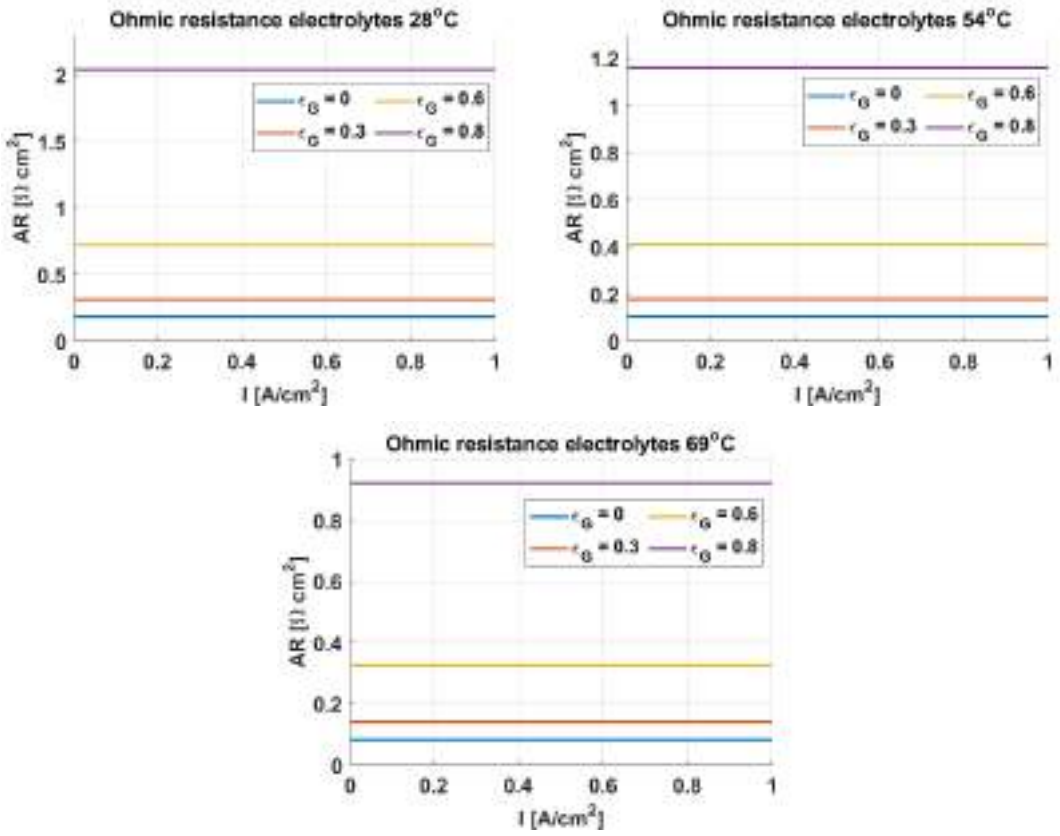

Figure 4.16: Calculated ohmic resistance due to electrolytes (33wt% NaOH and 25wt% NaCl) with different gas holdups at 28, 54 and 69°C, assuming a gap size of 0.25 mm on both sides. At 28, 54 and 69°C, the conductivities are 0.2455, 0.3815 and 0.4599 S/cm for NaCl and 0.3107, 0.6544 and 0.8925 S/cm for NaOH. Note: y-axis is different for all graphs.

It can be seen that even if the electrolyte is gas-free, a notable effect on the ohmic resistance is present due to the electrolytes, especially at lower temperature. It is also observed that if the gas holdup is around 0.3 or lower, the increase in ohmic resistance is minor. However, at high gas holdups (>0.6), a significant effect on the ohmic resistance is noticed. It is also observed that at low temperature, the effect of the gas holdup is stronger on the ohmic resistance than for higher temperatures. This is due to the lower conductivity of the electrolytes at low temperatures. Since it is observed that even at low temperatures the ohmic resistance seems constant with current density, this further supports the hypothesis that the bubbles do not affect the ohmic resistance significantly.

The experimentally deduced ohmic resistance will be compared to the membrane resistance according to Sijabat et al. It should be noted that Sijabat's data is not a perfect representation for the membrane resistance in the system used for this research, due to the fact that a different anolyte is being used; NaCl and NaOH for this work and Sijabat's work, respectively. When comparing the experimentally deduced ohmic resistance with the membrane resistance as reported by Sijabat et al, it can be seen that the membrane resistance is lower than the total ohmic resistance at higher temperatures, but the membrane resistance is higher than the total ohmic resistance at low temperature. Obviously, the total ohmic resistance cannot be lower than the membrane resistance. This indicates that the reported membrane resistance by Sijabat et al is not representable for the system used in this research. Either Sijabat's measurements could be slightly off, or the assumption that the NaCl concentration does not affect the membrane resistance is not valid. This discrepancy at low temperature also makes it difficult to draw strong conclusions at higher temperatures, since it is debatable whether the data from Sijabat is a sufficient representation for the membrane resistance of the system used for this research.

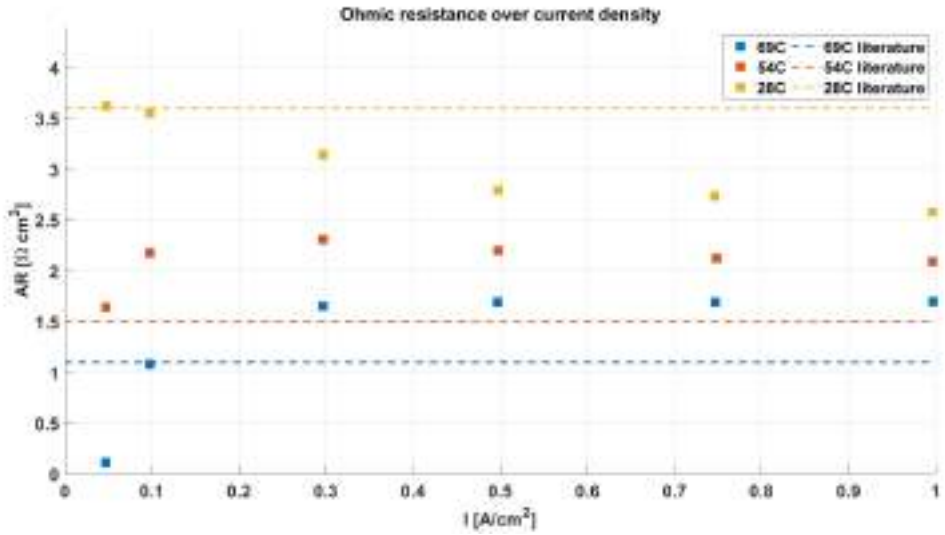

Figure 4.17: Experimentally determined ohmic resistances and membrane resistance according to Sijabat et al at 28, 54 and 69 °C. For complete list of experimental conditions, see Appendix F.

Overall, it seems like the ohmic resistance is relatively constant, indicating that bubbles have minor to no effects on the ohmic resistance of the cell. It is difficult to compare the ohmic resistance with the membrane resistance reported by Sijabat et al due to the unexpected discrepancy at low temperatures. Therefore, unfortunately, no clear conclusions can be drawn regarding the membrane resistance.

5. Conclusion

The bubble behavior in a zero-gap cell has been studied in this work. The use of a transparent Nafion 117 membrane allowed for visualization of the bubble behavior between the electrode and the membrane, which is unseen in literature. The main focus was on the hydrogen bubble behavior, because less chlorine bubbles are generated due to the higher solubility compared to hydrogen. This helps to not only better understand the chlor-alkali process, but also the AWE process due to the similarities for the cathodic side.

It was found that the bubble behavior can significantly differ per position. This can be attributed to the fact that the distance between the electrode and the membrane is not consistent along the reactor. At most positions, a bubble curtain of small hydrogen bubbles occurred inside the gap, indicating that there is sufficient amount of space available for these small bubbles to flow. When increasing the current density up to 66.7 mA/cm^2, a bubble froth could occur, which was quite immobile. At certain positions, static bubbles get trapped between the electrode and the membrane at low current densities (around 6.7 mA/cm^2). These bubbles reach diameters of around 0.2 - 0.3 mm while (seemingly) maintaining a spherical geometry. This suggests that the distance between the electrode and the membrane is around 0.2 - 0.3 mm. These static bubbles grow or get trapped at the same position. The removal of these static bubbles occurs via different mechanisms; coalescence with large bubbles in the openings, rise due to buoyancy or get pushed towards the openings due to capillary forces. When the current density is increased to 66.7 mA/cm^2, sliding bubbles and films are observed. These bubbles and films are pushed towards the rim of the openings in the cathode where the coalesce and form larger bubbles in the order of 0.4 - 0.7 mm diameter. These bubbles can then either detach or coalesce and form large bubbles ($>$ 3 mm diameter) occupying a significant fraction of a opening in the cathode. Upon detachment, these large hydrogen bubbles often leave a gas pocket behind between the electrode and membrane. From these gas pockets, new large bubbles start to grow. This behavior was not observed at the anodic side. Lastly, it was observed that also the backside of the cathode was active. After about 10 seconds of switching on the current at a current density of 6.7 mA/cm^2, bubbles started to nucleate on the backside of the cathode. One possible explanation for this phenomenon is that the current originally flows through the frontside of the electrode, since this is the shortest path, but after gas builds up between the electrode and the membrane the current starts to also flow via the backside of the electrode. Another explanation could be that it takes more time to reach the desired supersaturation at the backside in order to initiate bubble nucleation.

Less observations have been made for the anode, due to the earlier mentioned high solubility of chlorine. Nevertheless, a phenomenon indicating that the bubble behavior inside the gap is similar for both sides was observed. Sometimes bubbles suddenly appear at the rim of the openings in the anode. These bubbles pop out from the frontside of the electrode. This suggest that also at the anode, bubbles are growing inside the gap and being pushed towards the rim by capillary forces. Contrary to the cathode, no large bubbles occupying most of the openings are observed. At the anode small bubbles slide along the rim of the openings and collect at the top where they coalesce and form a larger bubble, until it detaches.

The electrochemical performance of the cell was also evaluated in order to determine whether this was affected by the bubble behavior. EIS was used to measure the combined Tafel slope and exchange current density. These values were then used to calculate the ohmic resistance over a current density range of 0.05 - 1 A/cm^2. The total overpotential according to the Tafel slope and exchange current density measured with EIS and the reversible cell potential are subtracted from the cell potential measured with the power supply. At higher current density ($>$ 0.3 A/cm^2), the ohmic resistance reached a relatively constant value. This indicates that the effect of bubbles on the ohmic resistance in a zero-gap configuration is minor. However, due to multiple assumptions that were made, such as the Tafel slope and exchange current density being independent of temperature, careful note should be taken when drawing this conclusion.

6. Recommendations for future work

This work helped to improve the understanding of bubble behavior in a zero-gap configuration. However, due to experimental limitations, indirect measuring techniques were required which increased the possibility of inaccuracies being introduced. Instead of directly measuring the ohmic resistance with the aid of EIS, an indirect calculation was used which required the (debatable) assumption of the Tafel slope and exchange current density being constant with temperature, current density as well as concentration. The first point of improvement that can be made, is using a high current potentiostat in order to measure the change in ohmic resistance over current density. The difficulty that comes with this technique is the fact that the cell has a large electrode area, making the system susceptible for small inaccuracies such as cable or contact resistances. Using a low resistance calibration set could help reducing these inaccuracies.

Since the membrane resistance measured by Sijabat et al at lower temperatures is higher than the experimentally found ohmic resistance, it is debatable whether Sijabat's results give an accurate indication of the membrane resistance employed for this research. In order to improve the reliability of these values, Sijabat's measurements could be carried out to see whether they are reproducible. Preferably, these measurements should be done for a NaCl-NaOH system instead of a NaOH-NaOH system, since it is unsure whether the assumption that the membrane resistance is independent of NaCl concentration, is valid. Alternative, more accurate, techniques compared to the one used by Sijabat et al, are proposed in literature [90]. Using these techniques could improve the accuracy of the membrane resistance.

Another limitation was the quality of the pump in the anolyte circuit. Due to an unreliable connection between the Teflon tubing and the Viton tubing in the peristaltic pump, only low flow rates could be used. It would be interesting to see the effect of the flow rate on both the bubble behavior as well as the electrochemical performance of the cell. Using a pump capable of reaching flow rates ranging from 0 to 20 mL/sec would be sufficient for this purpose.

More advanced image analysis techniques could be used to measure the bubble diameter or track the position of the bubbles over time. This could help with quantifying the electrode coverage and more accurately determining the gap size.

It might also be interesting to look at the bubble behavior with different electrode structures since, according to literature, the ohmic resistance can change with different morphologies [28]. By analyzing videos of bubble behavior with different structures, the origin of the difference could be explored. Also, the most ideal structure regarding performance can be found.

Even though the obtained videos and pictures were rather clear, improving the camera setup could help to better visualize the different phenomena occurring. Using a camera with a higher resolution and / or fps, optimizing the lighting positioning as well as stabilizing the camera setup could all help to improve the quality of the videos. For this work, all videos were made at the bottom quarter of the cell. To better understand the different phenomena occurring at different heights of the reactor, videos should be made along the height of the reactor.

Continuous replenishment of the electrolytes would give data more representative to industrial operation. Due to the recirculation of the electrolyte, the concentration changes over time which might affect the cell performance. Additionally, the electrolytes get saturated with their respective products, which could change the bubble effects over time. This effect is mainly relevant for the anolyte getting saturated with chlorine over time. This also causes the anolyte turning yellow/green over time which decreases the visibility of the cell.

7. Acknowledgements

Firstly, I would like to thank prof.dr.ir. John van der Schaaf for providing me with the opportunity to perform my master thesis at the SPE research group. You gave a lot of useful feedback during our meetings and ensured me to be critical with my results. I would also like to thank dr.ir Thijs de Groot for sparking my interest in the topic of electrochemistry. You shared your vast knowledge on the topic during our discussions which was very valuable. I would also like to express my gratitude to my daily supervisors PDEng. MSc R. Lira Garcia Barros, MSc N. Guruprasad and dr. C.F. Gomez. You helped me solving the struggles with the experimental setup (of which there were a lot) I was facing and you spend a lot of time helping me out with my research, for which I am sincerely grateful. Your broad knowledge helped me to widen my view. Lastly, I would like to thank S.G. van der Ven for keeping me sane during this research and helping me with solving all the issues we were facing. Your presence lightened the mood in the lab even though I sometimes was on the verge of a mental breakdown. You also provided a lot of feedback, even though you had to focus on your own research.

Nomenclature

Symbols

δ_{mem}	Thickness of membrane [cm]
ϵ_G	Gas holdup [$m^3{}_{gas}/m^3{}_{reactor}$]
ϵ_w	Dielectric constant of pure water [-]
η	Activation overpotential [V]
γ_i	Mean activity coefficient of component i [-]
κ	Conductivity [S/cm]
κ_0	Conductivity of pure electrolyte [S/cm]
λ	Equivalent conductivity at infinite dilution [S/cm]
ν	Stoichiometric coefficient [-]
Φ_m	Mass flow rate [g/s]
ρ_w	Density of water [-]
σ	Fractional covered area [-]
A	Area [cm^2]
A_ϕ	Debye-Hückel coefficient [-]
a_i	Activity of component i[-]
b	Tafel slope [mV/dec]
B_{MX}	Second virial-type coefficient [-]
b_{MX}	Modified pitzer model parameter [-]
c	Concentration [mol/L]
C_{MX}	Third virial-type coefficient [-]
d	Diameter [mm]
e	Electronic charge [C]
E_0	Thermodynamic potential [V]
E_{cell}	Total cell potential [V]
E_{rev}	Reversible cell potential [V]
E^0	Standard electrode potential [V]
F	Faraday constant [C/mol]
f^γ	Ionic strength function form of the Debye-Hückel term used for the activity coefficient [-]
I	Current density [A/cm^2]
I	Ionic strength [$mol/kg_{solvent}$]
I_0	Exchange current density [A/cm^2]

k_B	Boltzman constant [J/K]
m	Molality [mol/kg]
n	Number of moles [mol]
N_0	Avogadro constant [mol^{-1}]
$P_{H_2O}{}^{sat}$	Saturation pressure of water [mmHg]
P_i	Partial pressure of component i [bar]
$P_{total}{}^{i}$	Total pressure in compartment i [bar]
q_i	Modified pitzer model parameter [-]
R	Resistance [Ω]
R	Universal gas constant [J/K/mol]
R_i	The fractional lowering of vapor pressure due to the solute i [-]
s	Distance between electrode and membrane [cm]
T	Temperature [K]
T_c	Temperature [°C]
z	Ionic charge [-]

Superscripts and subscripts

A	Anodic
an	Anolyte
C	Cathodic
cath	Catholyte
M	Cation
mem	Membrane
MX	Neutral electrolyte
r	Reference
ref	Reference
tot	Total
X	Anion

References

[1] D. R. Kauffman, J. Thakkar, R. Siva, C. Matranga, P. R. Ohodnicki, C. Zeng and R. Jin, 'Efficient electrochemical co2 conversion powered by renewable energy,' *ACS Applied Materials and Interfaces*, vol. 7, no. 28, pp. 15 626–15 632, 2015. DOI: 10.1021/acsami.5b04393.

[2] R. Amirante, E. Cassone, E. Distaso and P. Tamburrano, 'Overview on recent developments in energy storage: Mechanical, electrochemical and hydrogen technologies,' *Energy Conversion and Management*, vol. 132, pp. 372–387, 2017. DOI: 10.1016/j.enconman.2016.11.046.

[3] Scopus. 'Scopus.' (), [Online]. Available: https://www.scopus.com/search/form.uri?display=basic#basic. (accessed:03-04-22).

[4] S. Lakshmanan and T. Murugesan, 'The chlor-alkali process: Work in progress,' *Clean Technologies and Environmental Policy*, vol. 16, no. 2, pp. 225–234, 2014. DOI: 10.1007/s10098-013-0630-6.

[5] G. G. Botte, 'Electrochemical manufacturing in the chemical industry,' *Electrochemical Society Interface*, vol. 23, no. 3, pp. 49–55, 2014. DOI: 10.1149/2.F04143if.

[6] K. Li, Q. Fan, H. Chuai, H. Liu, S. Zhang and X. Ma, 'Revisiting chlor-alkali electrolyzers: From materials to devices,' *Transactions of Tianjin University*, vol. 27, no. 3, pp. 202–216, 2021. DOI: 10.1007/s12209-021-00285-9.

[7] B. Alves. 'Global electricity consumption 1980-2019.' (), [Online]. Available: https://www.statista.com/statistics/280704/world-power-consumption/. (accessed:03-04-22).

[8] Covestro. 'Nominated: Energy-saving chlorine production.' (), [Online]. Available: https://www.covestro.com/press/nominated-energy-saving-chlorine-production/. (accessed:10-05-2022).

[9] Eurochlor. 'Uses.' (), [Online]. Available: https://www.eurochlor.org/uses/. (accessed:03-04-22).

[10] W. C. Council, 'The world chlorine council and sustainable development,' 2002. [Online]. Available: https://www.worldchlorine.org/wp-content/themes/brickthemewp/pdfs/report.pdf.

[11] M. Khandelwal and A. van Dril, 'Decarbonisation options for the dutch biofuels industry,' pp. 1–67, 2020. DOI: http://resolver.tudelft.nl/uuid:2cb38cb7-ce6b-40eb-8e05-8633cf4345d0.

[12] M. Succi, G. Macchi and S. R. Vogt, 'High purity hydrogen: Guidelines to select the most suitable purification technology,' *J. of Electrical Engineering*, vol. 5, no. 5, pp. 1–7, 2017. DOI: 10.17265/2328-2223/2017.05.005.

[13] Eurochlor. 'Hydrogen from chlor-alkali production: High purity, low carbon and available today.' (), [Online]. Available: https://www.eurochlor.org/news/hydrogen-from-chlor-alkali-production/. (accessed:03-04-22).

[14] H. Ito and A. Manabe, 'Chlor–alkali electrolysis,' *Electrochemical Power Sources: Fundamentals, Systems, and Applications*, pp. 281–304, 2022. DOI: 10.1016/b978-0-12-819424-9.00011-2.

[15] Corechem. 'Sodium hydroxide: Membrane vs diaphragm grade.' (), [Online]. Available: https://corecheminc.com/sodium-hydroxide-membrane-vs-diaphragm-grade/. (accessed:10-05-22).

[16] R. K. Karlsson and A. Cornell, 'Selectivity between oxygen and chlorine evolution in the chlor-alkali and chlorate processes,' *Chemical Reviews*, vol. 116, no. 5, pp. 2982–3028, 2016. DOI: 10.1021/acs.chemrev.5b00389.

[17] R. R. Sijabat., 'Intensified membrane electrolyzer: Maxwell-stefan modeling and experimental studies,' Ph.D. dissertation, Technische Universiteit Eindhoven, 2020.

[18] O. o. E. E. U.S. Department of Energy and R. Energy, 'Advanced chlor-alkali technology,' *Industrial Technologies Program*, vol. CPS 1797, pp. 1–2, 2004.

[19] T. Brinkmann, G. Giner Santonja, F. Schorcht, S. Roudier and L. Delgado Sancho, *Best Available Techniques Reference Document for the Production of Chlor-alkali*. 2014, ISBN: 9789279409455.

[20] A. T. Kuhn, *Industrial Electrochemical Processes*. Elsevier Publishing Company, 1971, ISBN: 9780444408853.

[21] J. Lee, A. Alam, C. Park, S. Yoon and H. Ju, 'Modeling of gas evolution processes in porous electrodes of zero-gap alkaline water electrolysis cells,' *Fuel*, vol. 315, pp. 123–273, 2022. DOI: 10.1016/j.fuel.2022.123273.

[22] M. Paidar, V. Fateev and K. Bouzek, 'Membrane electrolysis—history, current status and perspective,' *Electrochimica Acta*, vol. 209, pp. 737–756, 2016. DOI: 10.1016/j.electacta.2016.05.209.

[23] R. Phillips, A. Edwards, B. Rome, D. R. Jones and C. W. Dunnill, 'Minimising the ohmic resistance of an alkaline electrolysis cell through effective cell design,' *International Journal of Hydrogen Energy*, vol. 42, no. 38, pp. 23 986–23 994, 2017. DOI: 10.1016/j.ijhydene.2017.07.184.

[24] J. W. Haverkort and H. Rajaei, 'Voltage losses in zero-gap alkaline water electrolysis,' *Journal of Power Sources*, vol. 497, p. 229 864, 2021. DOI: 10.1016/j.jpowsour.2021.229864.

[25] J. Chin Kwie Joe, 'Aspects of power reduction in the chlor-alkali membrane electrolysis,' Ph.D. dissertation, Technische Universiteit Eindhoven, 1989. DOI: 10.6100/IR318621.

[26] E. Drioli and M. Nakagaki, *Membranes and membrane processes*. Plenum Publishers, 1986, ISBN: 9780306422706.

[27] M. T. de Groot and A. W. Vreman, 'Ohmic resistance in zero gap alkaline electrolysis with a zirfon diaphragm,' *Electrochimica Acta*, vol. 369, p. 137 684, 2021. DOI: 10.1016/j.electacta.2020.137684.

[28] R. Phillips, 'Zero gap cell design for alkaline electrolysis,' Ph.D. dissertation, Swansea University, 2019. DOI: 10.13140/RG.2.2.26663.29606.

[29] A. Angulo, P. van der Linde, H. Gardeniers, M. Modestino and D. Fernández Rivas, 'Influence of bubbles on the energy conversion efficiency of electrochemical reactors,' *Joule*, vol. 4, no. 3, pp. 555–579, 2020. DOI: 10.1016/j.joule.2020.01.005.

[30] H. Vogt and R. J. Balzer, 'The bubble coverage of gas-evolving electrodes in stagnant electrolytes,' *Electrochimica Acta*, vol. 50, no. 10, pp. 2073–2079, 2005. DOI: 10.1016/j.electacta.2004.09.025.

[31] J. R. Lake, Á. M. Soto and K. K. Varanasi, 'Impact of bubbles on electrochemically active surface area of microtextured gas-evolving electrodes,' *Langmuir*, vol. 38, no. 10, pp. 3276–3283, 2022. DOI: 10.1021/acs.langmuir.2c00035.

[32] R. Wüthrich, C. Comninellis and H. Bleuler, 'Bubble evolution on vertical electrodes under extreme current densities,' *Electrochimica Acta*, vol. 50, no. 25, pp. 5242–5246, 2005. DOI: 10.1016/j.electacta.2004.12.052.

[33] K. Thummar, R. Abang, K. Menzel and M. T. De Groot, 'Coupling a chlor-alkali membrane electrolyzer cell to a wind energy source: Dynamic modeling and simulations,' *Energies*, vol. 15, no. 2, 2022. DOI: 10.3390/en15020606.

[34] S. G. Bratsch, 'Standard electrode potentials and temperature coefficients in water at 298.15 k,' *Journal of Physical and Chemical Reference Data*, vol. 18, no. 1, pp. 1–21, 1989. DOI: 10.1063/1.555839.

[35] G. R. Salvi and A. J. DeBethune, 'The temperature coefficients of electrode potentials: Ii . the second isothermal temperature coefficient,' *Journal of the Electrochemical Society*, vol. 108, no. 7, p. 672, 1961. DOI: 10.1149/1.2428187.

[36] G. Faita, P. Longhi and T. Mussini, 'Standard potentials of the cl2/cl electrode at various temperatures with related thermodynamic functions,' *Journal of The Electrochemical Society*, vol. 114, no. 4, pp. 340–343, 1967. DOI: 10.1149/1.2426588.

[37] A. J. Bard, R. Parsons and J. Jordan, *Standard Potentials in Aqueous Solution*. CRC Press, 1985, ISBN: 9780824772918.

[38] T. O'Brien, T. V. Bommaraju and F. Hine, *Handbook of Chlor-Alkali Technology*. Springer US Boston, 2005, ISBN: 9780306486234.

[39] K. S. Pitzer, *Activity Coefficients in Electrolyte Solutions*. CRC Press, 1991, ISBN: 9781315890371.

[40] A. L. Rockwood, 'Meaning and measurability of single-ion activities, the thermodynamic foundations of ph, and the gibbs free energy for the transfer of ions between dissimilar materials,' *ChemPhysChem*, vol. 16, no. 9, pp. 1978–1991, 2015. DOI: 10.1002/cphc.201500044.

[41] F. Pérez-Villaseñr, G. A. Iglesias-Silva and K. R. Hall, 'Temperature dependence of a modified pitzer equation for strong electrolytes systems,' *Industrial and Engineering Chemistry Research*, vol. 42, no. 26, pp. 6962–6969, 2003. DOI: 10.1021/ie030251r.

[42] J. H. Van Der Stegen, H. Weerdenburg, A. J. Van Der Veen, J. A. Hogendoorn and G. F. Versteeg, 'Application of the pitzer model for the estimation of activity coefficients of electrolytes in ion selective membranes,' *Fluid Phase Equilibria*, vol. 157, no. 2, pp. 181–196, 1999. DOI: 10.1016/S0378-3812(99)00044-8.

[43] L. F. Silvester and K. S. Pitzer, 'Thermodynamics of geothermal brines. i. thermodynamic properties of vapor-saturated nacl (aq) solutions from 0-300c,' *University of California*, pp. 1–66, 1976. [Online]. Available: https://escholarship.org/uc/item/3rt171m7.

[44] C.-C. Chen, L. B. Evans, H. I. Britt and J. F. Boston, 'A local composition model for the excess gibbs energy of aqueous electrolyte systems,' *AIChE Journal*, vol. 32, no. 3, pp. 444–454, 1986. DOI: 10.1002/aic.690320311.

[45] G. Åkerlöf and G. Kegeles, 'Thermodynamics of concentrated aqueous solutions of sodium hydroxide,' *Journal of the American Chemical Society*, vol. 62, no. 3, pp. 620–640, 1940. DOI: 10.1021/ja01860a057.

[46] A. Lach, L. André, A. Lassin, M. Azaroual, J. P. Serin and P. Cézac, 'A new pitzer parameterization for the binary naoh-h2o and ternary naoh-nacl-h2o and naoh-lioh-h2o systems up to naoh solid salt saturation, from 273.15 to 523.15 k and at saturated vapor pressure,' *Journal of Solution Chemistry*, vol. 44, no. 7, pp. 1424–1451, 2015. DOI: 10.1007/s10953-015-0357-6.

[47] J. W. Åkerlöf Gösta Teare, 'Thermodynamics of concentrated aqueous solutions of hydrochloric acid,' *Journal of the American Chemical Society*, vol. 59, no. 10, pp. 1855–1868, 1937. DOI: 10.1021/ja01289a021.

[48] C. Malmberg and A. Maryott, 'Dielectric constant of water from 0 to 100 c,' *Journal of Research of the National Bureau of Standards*, vol. 56, no. 1, pp. 1–8, 1956. DOI: 10.6028/jres.056.001.

[49] C. B. Alcock and G. W. Hooper, 'Thermodynamics of the gaseous oxides of the platinum-group metals,' *Proceedings of the Royal Society of London. Series A. Mathematical and Physical Sciences*, vol. 254, no. 1279, pp. 551–561, 1960. DOI: 10.1098/rspa.1960.0040.

[50] R. B. MacMullin, 'Algorithms for vapor pressure of water over aqueous solutions of salt and caustic soda,' *Journal of The Electrochemical Society*, vol. 116, no. 3, pp. 416–419, 1969. DOI: 10.1149/1.2411864.

[51] D. Roizard, *Encyclopedia of Membranes*, ser. 2. Springer Berlin Heidelberg, 2014, ISBN: 9783642408724.

[52] W. Wang, X. Wei, D. Choi, X. Lu, G. Yang and C. Sun, *Advances in Batteries for Medium and Large-Scale Energy Storage*. Woodhead Publishing, 2014, ISBN: 9781782420224.

[53] E. J. Dickinson and A. J. Wain, 'The butler-volmer equation in electrochemical theory: Origins, value, and practical application,' *Journal of Electroanalytical Chemistry*, vol. 872, p. 114 145, 2020. DOI: 10.1016/j.jelechem.2020.114145.

[54] D. A. Noren and M. A. Hoffman, 'Clarifying the butler-volmer equation and related approximations for calculating activation losses in solid oxide fuel cell models,' *Journal of Power Sources*, vol. 152, no. 2, pp. 175–181, 2005. DOI: 10.1016/j.jpowsour.2005.03.174.

[55] F. Franco, J. Prior, S. Velizarov and A. Mendes, 'A systematic performance history analysis of a chlor-alkali membrane electrolyser under industrial operating conditions,' *Applied Sciences*, vol. 9, no. 284, pp. 1–11, 2019. DOI: 10.3390/app9020284.

[56] B. V. Tilak, 'Kinetics of chlorine evolution—a comparative study,' *Journal of The Electrochemical Society*, vol. 126, no. 8, pp. 1343–1348, 1979. DOI: 10.1149/1.2129274.

[57] J. F. Silva, A. C. Dias, P. Araújo, C. M. Brett and A. Mendes, 'Electrochemical cell design for the impedance studies of chlorine evolution at dsa® anodes,' *Review of Scientific Instruments*, vol. 87, no. 8, 2016. DOI: 10.1063/1.4959097.

[58] L. J. Janssen, L. M. Starmans, J. G. Visser and E. Barendrecht, 'Mechanism of the chlorine evolution on a ruthenium oxide/titanium oxide electrode and on a ruthenium electrode,' *Electrochimica Acta*, vol. 22, no. 10, pp. 1093–1100, 1977. DOI: 10.1016/0013-4686(77)80045-5.

[59] J. A. Harrison, D. L. Caldwell and R. E. White, 'Electrocatalysis and the chlorine evolution reaction-ii. comparison of anode materials,' *Electrochimica Acta*, vol. 29, no. 2, pp. 203–209, 1984. DOI: 10.1016/0013-4686(84)87048-6.

[60] T. A. Lassali, J. F. Boodts and S. Trasatti, 'Electrocatalytic activity of the ternary oxide ru0.3ptxti(0.7 - x)o2 for chlorine evolution,' *Electrochimica Acta*, vol. 39, no. 11, pp. 1545–1549, 1994. DOI: 10.1016/0013-4686(94)85133-6.

[61] S. V. Evdokimov, 'Kinetics of chlorine evolution on dimensionally stable anodes at high currents: Extending the concept of a self-accelerating electrode process,' *Russian Journal of Electrochemistry*, vol. 36, no. 3, pp. 236–239, 2000. DOI: 10.1007/BF02827966.

[62] N. Krstajić, M. Popović, B. Grgur, M. Vojnović and D. Šepa, 'On the kinetics of the hydrogen evolution reaction on nickel in alkaline solution - part i. the mechanism,' *Journal of Electroanalytical Chemistry*, vol. 152, no. 1, pp. 16–26, 2001. DOI: 10.1016/S0022-0728(01)00590-3.

[63] N. Krstajić, M. Popović, B. Grgur, M. Vojnović and D. Šepa, 'On the kinetics of the hydrogen evolution reaction on nickel in alkaline solution: Part ii. effect of temperature,' *Journal of Electroanalytical Chemistry*, vol. 152, no. 1, pp. 16–26, 2001. DOI: 10.1016/S0022-0728(01)00590-3.

[64] F. Bao, E. Kemppainen, I. Dorbandt, R. Bors, F. Xi, R. Schlatmann, R. van de Krol and S. Calnan, 'Understanding the hydrogen evolution reaction kinetics of electrodeposited nickel-molybdenum in acidic, near-neutral, and alkaline conditions,' *ChemElectroChem*, vol. 8, no. 1, pp. 195–208, 2021. DOI: 10.1002/celc.202001436.

[65] M. H. Miles, G. Kissel, P. W. T. Lu and S. Srinivasan, 'Effect of temperature on electrode kinetic parameters for hydrogen and oxygen evolution reactions on nickel electrodes in alkaline solutions,' *Journal of The Electrochemical Society*, vol. 123, no. 3, pp. 332–336, 1976. DOI: 10.1149/1.2132820.

[66] J. L. Weininger and M. W. Breiter, 'Hydrogen evolution and surface oxidation of nickel electrodes in alkaline solution,' *Journal of The Electrochemical Society*, vol. 111, no. 6, pp. 707–712, 1964. DOI: 10.1149/1.2426216.

[67] M. C. Monteiro, A. Goyal, P. Moerland and M. T. Koper, 'Understanding cation trends for hydrogen evolution on platinum and gold electrodes in alkaline media,' *ACS Catalysis*, vol. 11, no. 23, pp. 14 328–14 335, 2021. DOI: 10.1021/acscatal.1c04268.

[68] W. Sheng, M. Myint, J. G. Chen and Y. Yan, 'Correlating the hydrogen evolution reaction activity in alkaline electrolytes with the hydrogen binding energy on monometallic surfaces,' *Energy and Environmental Science*, vol. 6, no. 6, pp. 1509–1512, 2013. DOI: 10.1039/c3ee00045a.

[69] H. Vogt, 'The quantities affecting the bubble coverage of gas-evolving electrodes,' *Electrochimica Acta*, vol. 235, pp. 495–499, 2017. DOI: 10.1016/j.electacta.2017.03.116.

[70] C. W. M. P. Sillen, 'The effect of gas bubble evolution on the energy efficiency in water electrolysis,' Ph.D. dissertation, Technische Hogeschool Eindhoven, 1983. DOI: 10.6100/IR40592.

[71] D. Kiuchi, H. Matsushima, Y. Fukunaka and K. Kuribayashi, 'Ohmic resistance measurement of bubble froth layer in water electrolysis under microgravity,' *Journal of The Electrochemical Society*, vol. 153, no. 8, pp. 138–143, 2006. DOI: 10.1149/1.2207008.

[72] X. Zhao, H. Ren and L. Luo, 'Gas bubbles in electrochemical gas evolution reactions,' *Langmuir*, vol. 35, no. 16, pp. 5392–5408, 2019. DOI: 10.1021/acs.langmuir.9b00119.

[73] P. G. Mendoza, 'Intensification of the chlor-alkali process using a rotor-stator spinning disc membrane electrochemical reactor,' Ph.D. dissertation, Technische Hogeschool Eindhoven, 2016.

[74] J. Dukovic and C. W. Tobias, 'Influence of attached bubbles on potential drop and current distribution at gas-evolving electrodes,' *Journal of The Electrochemical Society*, vol. 134, no. 2, pp. 122–147, 1987. DOI: 10.1149/1.2100456.

[75] P. J. Sides and C. W. Tobias, 'Primary potential and current distribution around a bubble on an electrode.,' *Journal of The Electrochemical Society*, vol. 127, no. 2, pp. 277–270, 1980. DOI: 10.1149/1.2129657.

[76] I. A. Stenina, P. Sistat, A. I. Rebrov, G. Pourcelly and A. B. Yaroslavtsev, 'Ion mobility in nafion-117 membranes,' *Desalination*, vol. 170, no. 1, pp. 49–57, 2004. DOI: 10.1016/j.desal.2004.02.092.

[77] M. Cappadonia, J. W. Erning, S. M. Niaki and U. Stimming, 'Conductance of nafion 117 membranes as a function of temperature and water content,' *Solid State Ionics*, vol. 77, pp. 65–69, 1995. DOI: 10.1016/0167-2738(94)00289-5.

[78] R. R. Chandran and D. T. Chin, 'Reactor analysis of a chlor-alkali membrane cell.,' *Electrochimica Acta*, vol. 31, no. 1, pp. 39–50, 1986. DOI: 10.1016/0013-4686(86)80058-5.

[79] R. R. Chandran, R. S. Yeo and D. T. Chin, 'Sorption and transport behavior of perfluorinated ionomer membranes in concentrated naoh solution,' *Electrochimica Acta*, vol. 30, no. 12, pp. 1585–1590, 1985. DOI: 10.1016/0013-4686(85)87003-1.

[80] A. K. Chemicals. 'Recent development of asahi kasei chemicals 's im technology.' (), [Online]. Available: https://vdocuments.mx/07asahikaseichemicals.html. (accessed:10-06-22).

[81] M. M. Silver and E. M. Spore, *Proceedings of the Symposium on Advances in the Chlor-Alkali and Chlorate Industry*. Industrial Electrolytic Division, Electrochemical Society, 1984.

[82] D. Zhang and K. Zeng, 'Evaluating the behavior of electrolytic gas bubbles and their effect on the cell voltage in alkaline water electrolysis,' *Industrial and Engineering Chemistry Research*, vol. 51, no. 42, pp. 13 825–13 832, 2012. DOI: 10.1021/ie301029e.

[83] D. Vervaecke, 'Complete force balance analysis in electrolytic bubbles,' Ph.D. dissertation, Technische Universiteit Eindhoven, 2021.

[84] I. M. E. Hoedemakers, 'Study of the bubble behavior in alkaline water electrolysis,' Ph.D. dissertation, Technische Universiteit Eindhoven, 2020.

[85] T. Le Luu, J. Kim and J. Yoon, 'Physicochemical properties of ruo2 and iro2 electrodes affecting chlorine evolutions,' *Journal of Industrial and Engineering Chemistry*, vol. 21, pp. 400–404, 2015. DOI: 10.1016/j.jiec.2014.02.052.

[86] R. Sigwadi, M. S. Dhlamini, T. Mokrani and F. Nemavhola, 'Enhancing the mechanical properties of zirconia/nafion® nanocomposite membrane through carbon nanotubes for fuel cell application,' *Heliyon*, vol. 5, no. 7, 2019. DOI: 10.1016/j.heliyon.2019.e02112.

[87] S. Goswami, S. Klaus and J. Benziger, 'Wetting and absorption of water drops on nafion films,' *Langmuir*, vol. 24, no. 16, pp. 8627–8633, 2008. DOI: 10.1021/la800799a.

[88] A. C. de Bastos Vidal Dias, 'Chlor-alkali membrane cell process: Study and characterization,' Ph.D. dissertation, University of Porto, 2010. DOI: 10.6100/IR318621.

[89] Z. Y. C. Chuansin, 'Study on the hydrophilicity of nafion membrane surface,' *Journal of Electrochemistry*, vol. 3, no. 1, pp. 45–49, 1997. [Online]. Available: http://electrochem.xmu.edu.cn/EN/Y1997/V3/I1/45.

[90] J. Rodríguez, S. Palmas, M. Sánchez-Molina, E. Amores, L. Mais and R. Campana, 'Simple and precise approach for determination of ohmic contribution of diaphragms in alkaline water electrolysis,' *Membranes*, vol. 9, no. 10, 2019. DOI: 10.3390/membranes9100129.

[91] R. J. Gilliam, J. W. Graydon, D. W. Kirk and S. J. Thorpe, 'A review of specific conductivities of potassium hydroxide solutions for various concentrations and temperatures,' *International Journal of Hydrogen Energy*, vol. 32, no. 3, pp. 359–364, 2007. DOI: 10.1016/j.ijhydene.2006.10.062.

[92] W. R. Bousfield and T. M. Lowry, 'The electrical conductivity and other properties of sodium hydroxide in aqueous solution, as elucidating the mechanism of conduction,' *Philosophical Transactions of the Royal Society of London Series A*, vol. 74, pp. 253–322, 1905. DOI: 10.1098/rsta.1905.0007.

[93] A. L.-W. Woo, 'Conductance studies of concentrated solutions of sodium hydroxide and potassium hydroxide electrolytes,' Ph.D. dissertation, South Dakota State University, 1968.

[94] R. E. Davis and G. L. Horvath, 'The solubility and diffusion coefficient of oxygen in potassium hydroxide solutions,' *Electrochimica Acta*, vol. 12, no. 3, pp. 287–297, 1967. DOI: 10.1016/0013-4686(67)80007-0.

[95] N. Yokota, 'Solubilities of chlorine in concentrated sodium chloride solution,' *Chemical engineering*, vol. 22, no. 8, pp. 476–482, 1958. DOI: 10.1252/kakoronbunshu1953.22.476.

Appendix

A. Standard Electrode Potential

The standard electrode potentials and their temperature coefficients [34]. Bratsch only provided the values for the half reactions at pH = 0.000 and pH = 13.996, which is not entirely true for the chlor-alkali process. Nevertheless, the values at pH = 0.000 will be used for the anodic standard electrode potential and the values at pH = 13.996 will be used for the cathodic standard electrode potential. These values are compared with additional literature to validate their reliability. The discrepancies over the range of 25 to 100°C are small. The standard electrode potential for hydrogen evolution showed a maximum deviation of 0.81mV [35], and for chlorine evolution a maximum deviation of 1.8mV was found [36][37].

$$E^0_{A,T} = E^0_{A,298} + (T - 298.15)\left(\frac{dE^0_A}{dT}\right)_{298} + 0.5(T - 298.15)^2\left(\frac{d^2E^0_A}{dT^2}\right)_{298} \tag{1}$$

$$E^0_{A,298} = 1.3604 \text{ V}, \quad \left(\frac{dE^0_A}{dT}\right)_{298} = -1.248 \text{ mV/K}, \quad \left(\frac{d^2E^0_A}{dT^2}\right)_{298} = -5.83 \ \mu\text{V/K}^2 \tag{2}$$

$$E^0_{C,T} = E^0_{C,298} + (T - 298.15)\left(\frac{dE^0_C}{dT}\right)_{298} + 0.5(T - 298.15)^2\left(\frac{d^2E^0_C}{dT^2}\right)_{298} \tag{3}$$

$$E^0_{C,298} = -0.828 \text{ V}, \quad \left(\frac{dE^0_A}{dT}\right)_{298} = -0.8360 \text{ mV/K}, \quad \left(\frac{d^2E^0_A}{dT^2}\right)_{298} = -7.78 \ \mu\text{V/K}^2 \tag{4}$$

B. Antoines coefficients

The coefficients for the Antoine equation for water in the temperature range of 1-99C [51].

Coefficient	Value
A	8.07131
B	1730.63
C	233.426

Table 1: Antoines coefficients

C. Pitzer model for NaCl

The empirical constants of the modified Pitzer model for NaCl are listed in the table below [41].

Variable	Value
b_{mx}	2.22718
q_1	$5.383 \cdot 10^{-2}$
q_2	$1.54152 \cdot 10^{-2}$
q_3	$-3.15788 \cdot 10^{-5}$
q_4	0
q_5	$4.00346 \cdot 10^{-11}$
q_6	$1.34 \cdot 10^{-3}$
q_7	$-1.51455 \cdot 10^{-3}$
q_8	$3.19312 \cdot 10^{-6}$
q_9	0
q_{10}	$-4.33948 \cdot 10^{-12}$

Table 2: Pitzer model emperical constants

D. NaOH conductivity

Since no accurate conductivity correlation for NaOH is present in literature, experimental data will be empirically fitted. The conductivity of NaOH shows a similar trend to KOH, therefore it is decided to fit the experimental data to an empirical correlation that describes the KOH conductivity precisely [91]. The coefficients of this equation will be fitted according to the nonlinear least-squares method in MATLAB.

$$\kappa_{NaOH} = Am + Bm^2 + CmT + D\frac{m}{T} + Em^3 + Fm^2T^2 \tag{5}$$

With κ, M and T in S/m, mol/L and K, respectively. The data from literature presents the conductivity at 0, 18, 50 and 100C and concentrations ranging from 1 to 14.17 mol/L [92].

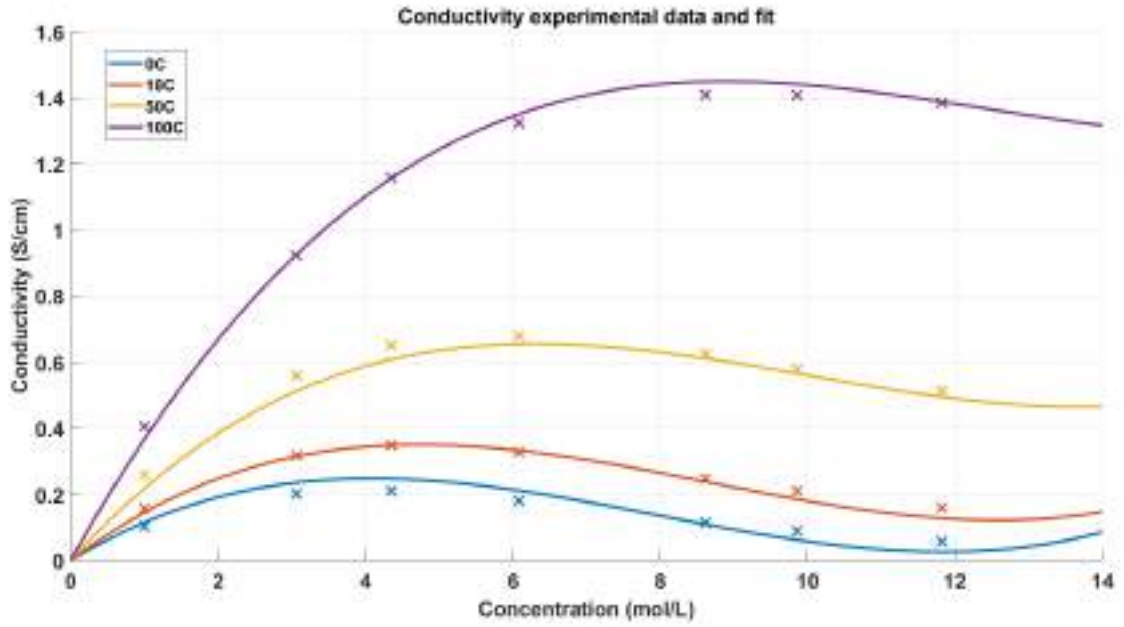

Figure 1: Conductivity of NaOH vs concentration at different temperatures. Experimental data and fit.

The fitted empirical equation was also compared with experimental data from additional literature [93].

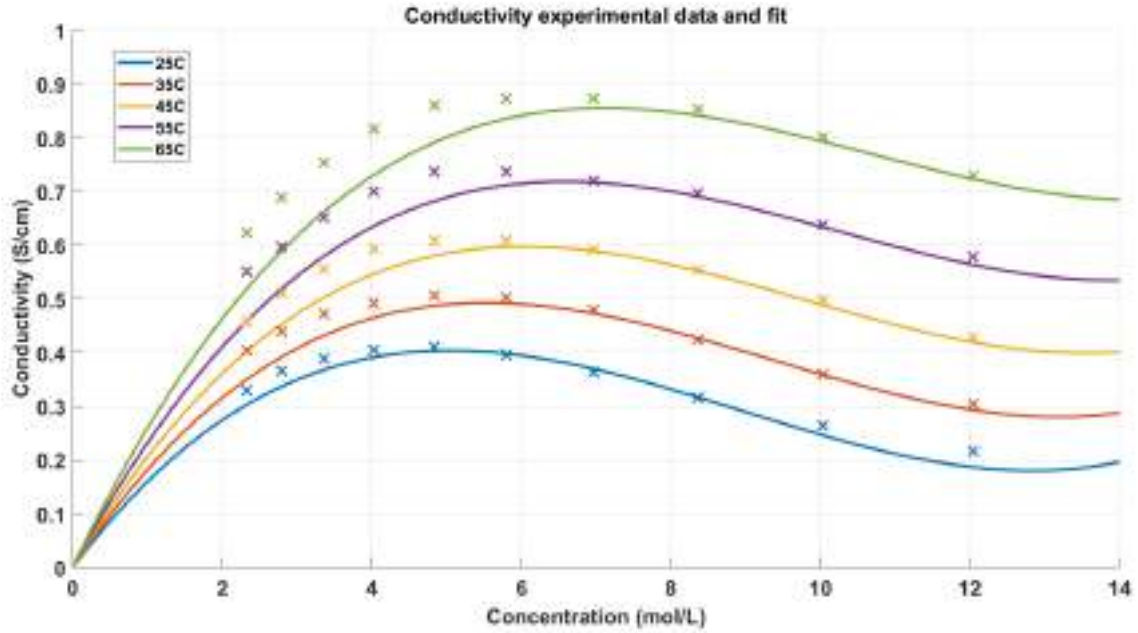

Figure 2: Conductivity of NaOH vs concentration at different temperatures. Experimental data from additional literature and fit.

When comparing the fit with the experimental data, it can be seen that the experimental values are best predicted at higher concentrations, especially for high temperatures. Since this is in the industrial relevant regime, it is decided that this fit is acceptable. The empirically fitted values are tabulated below.

Coefficient	Value
A	-2.5541
B	$-8.1781 \cdot 10^{-3}$
C	$5.6885 \cdot 10^{-3}$
D	310.8739
E	$9.4795 \cdot 10^{-4}$
F	$-1.9428 \cdot 10^{-7}$

Table 3: NaOH conductivity fitting parameters

E. P&ID

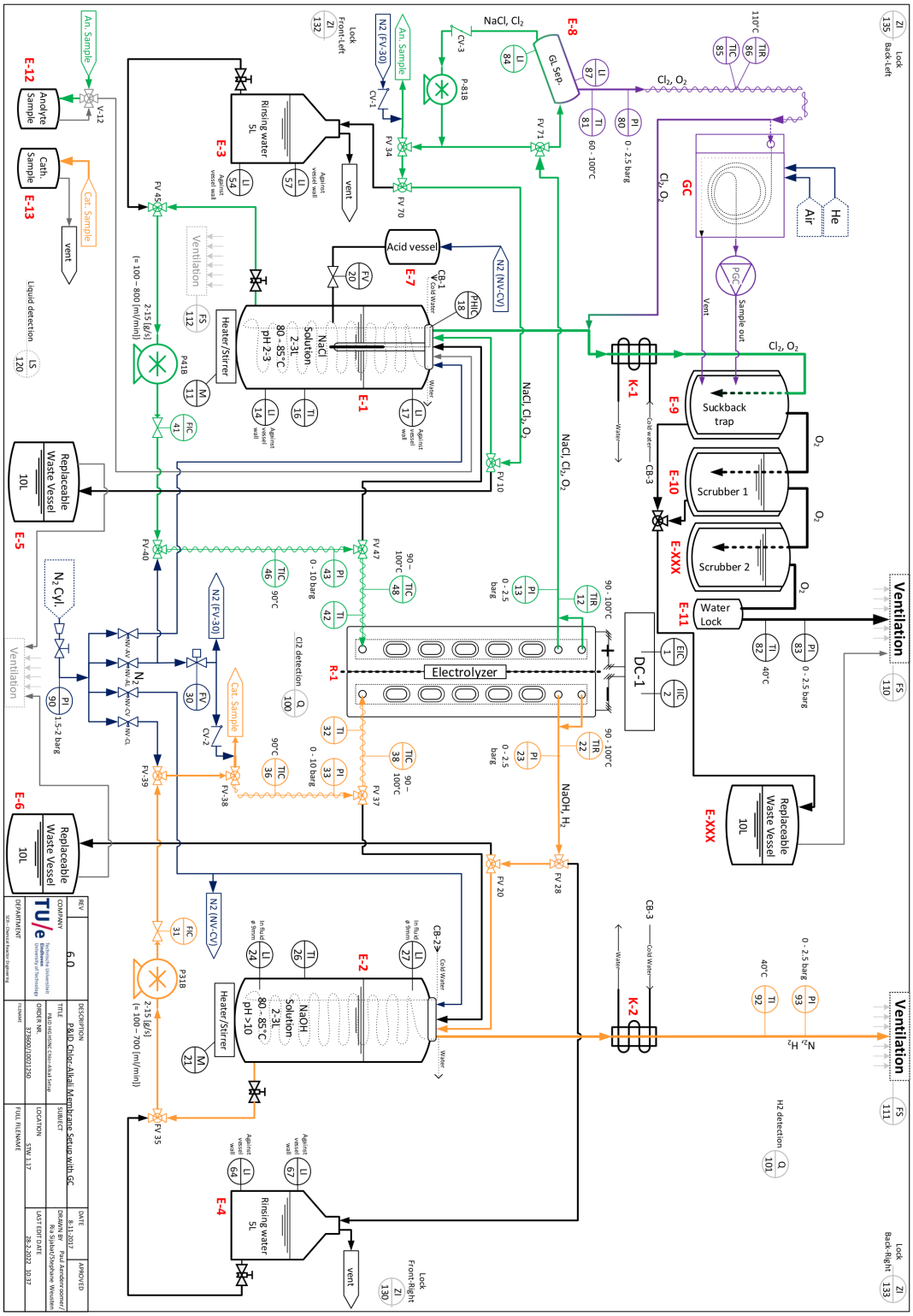

Figure 3: P&ID of the chlor-alkali setup

F. Experimental polarization curve conditions

T (K)	NaOH (wt%)	NaCl (wt%)	E_{rev}	$\Phi_{m,A}$ (g/s)	$\Phi_{m,C}$ (g/s)
301	33.3	16.8	2.2862	4	4
327	33.9	25.7	2.2502	4	4
342	32.5	26.0	2.2311	4	4

Table 4: Polarization curve conditions

G. Nyquist plots

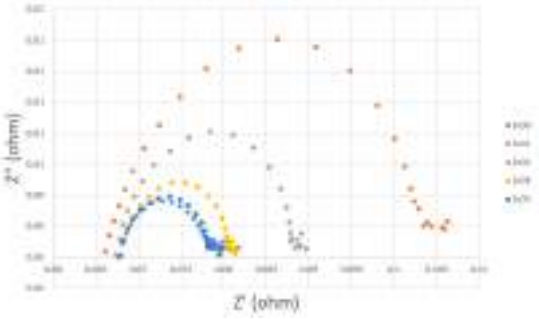

Figure 4: Nyquist plots at 0.01, 0.02, 0.04 0.05 and 0.06 A/cm^2.

I (A/cm^2)	R_1 (Ω)	R_2 (Ω)	Q (s^N/Ω)	N (-)
0.01	$6.64 \cdot 10^{-2}$	$3.79 \cdot 10^{-2}$	$4.79 \cdot 10^{-1}$	$8.06 \cdot 10^{-1}$
0.02	$6.76 \cdot 10^{-2}$	$2.11 \cdot 10^{-2}$	$3.86 \cdot 10^{-1}$	$8.43 \cdot 10^{-1}$
0.04	$6.81 \cdot 10^{-2}$	$1.29 \cdot 10^{-2}$	$4.13 \cdot 10^{-1}$	$8.38 \cdot 10^{-1}$
0.05	$6.81 \cdot 10^{-2}$	$1.03 \cdot 10^{-2}$	$3.73 \cdot 10^{-1}$	$8.56 \cdot 10^{-1}$
0.06	$6.78 \cdot 10^{-2}$	$1.03 \cdot 10^{-2}$	$6.28 \cdot 10^{-1}$	$8.01 \cdot 10^{-1}$

Table 5: Nyquist plot fitting parameters

H. Density

The temperature and concentration dependent densities of NaOH and NaCl can be found below, where W_x is the weight percentage of component x and Tc is the temperature in °C [17].

NaOH

$$\rho_{NaOH} = Q_{NaOH} + R_{NaOH} \cdot W_{NaOH} + S_{NaOH} \cdot W_{NaOH}^2 + T_{NaOH} \cdot W_{NaOH}^3 \tag{6}$$

$$Q_{NaOH} = 1.00224925 - 0.116831975 \cdot 10^{-3} \cdot Tc - 0.3210971 \cdot 10^{-5} \cdot Tc^2 \tag{7}$$

$$R_{NaOH} = 0.01148599 - 0.319841025 \cdot 10^{-4} \cdot Tc + 0.21510285 \cdot 10^{-6} \cdot Tc^2 \tag{8}$$

$$S_{NaOH} = 0.19658565 \cdot 10^{-5} + 0.761527825 \cdot 10^{-6} \cdot Tc - 0.61560685 \cdot 10^{-8} \cdot Tc^2 \tag{9}$$

$$T_{NaOH} = -0.33469112 - 0.7552771 \cdot 10^{-8} \cdot Tc + 0.661632323 \cdot 10^{-10} \cdot Tc^2 \tag{10}$$

NaCl

$$\rho_{NaCl} = Q_{NaCl} + R_{NaCl} \cdot W_{NaCl} + S_{NaCl} \cdot W_{NaCl}^2 \tag{11}$$

$$Q_{NaCl} = 1.0004075 - 0.71687895 \cdot 10^{-5} \cdot Tc - 0.51792075 \cdot 10^{-5} \cdot Tc^2 + 0.1054032 \cdot 10^{-7} \cdot Tc^3 \tag{12}$$

$$R_{NaCl} = 0.0074569085 - 0.2960572 \cdot 10^{-4} \cdot Tc + 0.30564225 \cdot 10^{-6} \cdot Tc^2 - 0.934493315 \cdot 10^{-9} \cdot Tc^3 \tag{13}$$

$$S_{NaCl} = 0.18372605 \cdot 10^{-4} + 0.42360185 \cdot 10^{-6} \cdot Tc - 0.51483125 \cdot 10^{-8} \cdot Tc^2 + 0.1794537 \cdot 10^{-10} \cdot Tc^3 \tag{14}$$

I. Viscosity

The temperature and concentration dependent viscosity's of NaOH and NaCl can be found below, where x_x is the weight fraction of component x and Tc is the temperature in °C [17]. Both require the viscosity of the solvent, which is water in this case.

$$\eta_{H_2O} = \frac{(Tc + 246)}{(0.05594 \cdot Tc + 5.2842) \cdot Tc + 137.37} \tag{15}$$

NaOH

$$\eta_{solute,NaOH} = exp\left(\frac{440.2 \cdot x_{NaOH}^{0.0089764} - 423.67}{(0.015949 \cdot Tc + 1) \cdot (107.6 x_{NaOH}^{4.6489}) + 1}\right) \tag{16}$$

$$\eta_{NaOH} = \eta_{solute,NaOH}^{x_{NaOH}} \cdot \eta_{H_2O}^{1-x_{NaOH}} \tag{17}$$

NaCl

$$\eta_{solute,NaCl} = exp\left(\frac{16.222 \cdot x_{NaCl}^{1.3229} + 1.4849}{(0.0074691 \cdot Tc + 1) \cdot (30.78 x_{NaCl}^{2.0583}) + 1}\right) \tag{18}$$

$$\eta_{NaCl} = \eta_{solute,NaCl}^{x_{NaCl}} \cdot \eta_{H_2O}^{1-x_{NaCl}} \tag{19}$$

J. Solubility

Oxygen

The solubility of oxygen in KOH at room temperature is given by the following equation [94].

$$log(S) = log(1.26 \cdot 10^{-3}) - 0.1746 \cdot C \tag{20}$$

Where S is the solubility of oxygen in mol/L and C is the concentration of KOH in mol/L.

Chlorine

The Henry constant for chlorine in acidic NaCl can be calculated according to the following correlation [95].

$$H_c = (2.21 - 0.00398[NaCl]) \cdot 10^{-5} \cdot 10^{1000/T} \tag{21}$$

With [NaCl] in g/L, T in K and H_c in mol/L atm